Electronic Supplementary Material (ESI) for Chemical Communications.
This journal is © The Royal Society of Chemistry 2021

Electronic Supplementary Information

Fusing pyrene and ferrocene into a chiral, redox-active triangle

Marvin Metzelaars,[a] Sergio Sanz,[b] Jeff Rawson,[†ab] Rudolf Hartmann,[c] Claus M. Schneider[b] and Paul Kögerler*[ab]

[a] *Institute of Inorganic Chemistry, RWTH Aachen University, 52074 Aachen, Germany.*

[b] *Peter Grünberg Institute (PGI-6), Forschungszentrum Jülich GmbH, 52425 Jülich, Germany.*

[c] *Institute of Biological Information Processing (IBI-7), Forschungszentrum Jülich GmbH, 52425 Jülich, Germany.*

† present address: Department of Chemistry and Chemical Biology, Harvard University, Cambridge, MA 02138, USA.

* corresponding author; Email: paul.koegerler@ac.rwth-aachen.de

Acknowledgments

The authors acknowledge access to the Jülich-Düsseldorf Biomolecular NMR Center that is jointly run by Forschungszentrum Jülich and Heinrich-Heine-Universität Düsseldorf. We thank Dr Gerhard Fink (RWTH Aachen University) and Dr Sabine Willbold (Research Centre Jülich) for performing variable-temperature NMR experiments.

Table of Contents

Materials and Methods

All reactions were carried out using standard Schlenk line and glove box techniques (Ar atmosphere), while work-up was performed under ambient conditions. Pyrene (Py) and ferrocene (Fc) were purified by column chromatography (SiO_2, eluent: *n*-hexane) and sublimation, respectively. Other commercial chemicals were used as received. 1,1'-Bis(di-*tert*-butylphosphino)ferrocene]dichloropalladium(II) ($PdCl_2$(dtbpf)) (99%, abcr) was stored in an Ar glove box at –40 °C. Drying of *N*,*N*-dimethylformamide (DMF) was achieved by vacuum distillation over $CaSO_4$ and storage over a molecular sieve under Ar. The starting materials pyrene-2,7-bis(4,4,5,5-tetramethyl-1,3,2-dioxaborolan) (2,7-bis(Bpin)pyrene),[1] iodoferrocene,[2] and 1,1'-diiodoferrocene[2] were synthesised as previously reported. Ultraviolet-visible near-infrared (UV-Vis-NIR) absorption spectra were measured on a Shimadzu UV-3600 plus spectrophotometer using 10 mm quartz glass cuvettes (QS, Hellma Analytics). Oxidation experiments were performed under inert conditions by using a screw-cap cuvette that was filled with sample solution in an Ar glovebox. A stock solution of $AgBF_4$ or $AgSbF_6$ prepared in anhydrous dichloromethane (CH_2Cl_2) was added stepwise to the cuvette containing the sample solution. After each addition step, a UV-Vis-NIR spectrum was recorded after transfer of the sealed cuvette from the glovebox to the spectrometer. Circular dichroism (CD) was measured on a J-1100 CD spectrophotometer (JASCO). Elemental analysis (C, H, N) was performed on a vario EL cube (elementar) with thermal conductivity detector. Matrix-assisted laser desorption/ionisation (MALDI) high-resolution mass spectrometry (HRMS) experiments were performed on a Thermo Scientific MALDI LTQ Orbitrap XL mass spectrometer. Small quantities of sample and matrix were individually dissolved in CH_2Cl_2 or tetrahydrofuran (THF), mixed prior to dropping on a stainless-steel target plate and dried under ambient conditions. Tetracyanoquinodimethane (TCNQ) and 4'-hydroxyazobenzene-2-carboxylic acid (HABA) were used as matrix, providing the same qualitative results. Measurements were performed in positive ion mode. Nuclear magnetic resonance (NMR) experiments at room temperature were performed on a Bruker Avance III HD 600 MHz NMR spectrometer equipped with a CryoProbe Prodigy. The spectra were recorded in chloroform-d1 or toluene-d8 and referenced to residual solvent peaks. Variable temperature (VT) NMR experiments (400 MHz) were performed in dichloromethane-d2 on a Bruker Avance II 400 MHz NMR spectrometer. The temperature control was realised using a nitrogen gas flow, precooled with liquid nitrogen and temperature control unit (BVT3200). VT-NMR (800 MHz), TOCSY and ROESY 2D-NMR spectra were measured on an 800 MHz Bruker Avance III HD NMR spectrometer equipped with a TXI RT-probe. Room temperature NMR, elemental analysis of **1** and

HRMS measurements were performed by the Central Institute for Engineering, Electronics and Analytics (ZEA-3), Forschungszentrum Jülich GmbH (52425 Jülich, Germany). The 800 MHz VT- and 2D-NMR experiments were performed by the NMR department of the Institute for Biological Information Processing (IBI-7), Forschungszentrum Jülich GmbH (52425 Jülich, Germany).

Syntheses

Synthesis of 2-ferrocenylpyrene ***1***

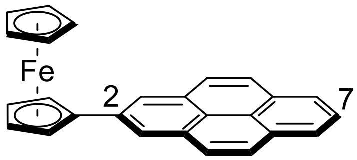

2-(Bpin)pyrene (0.500 g, 1.5 mmol, 1 eq.), iodoferrocene (0.425 g, 2.3 mmol, 1.5 eq.), $PdCl_2$(dtbpf) (49.6 mg, 0.08 mmol, 0.05 eq.) and K_3PO_4 (1.293 g, 6.1 mmol, 3 eq.) were suspended in anhydrous DMF (80 mL) and stirred at 60 °C for 24 h. The cooled reaction mixture was diluted with water and CH_2Cl_2. The organic phase was separated and thoroughly washed with brine. The combined organic phase was dried over $MgSO_4$ and solvent evaporated under reduced pressure. The product mixture was pushed through a silica plug (silica gel; eluent: CH_2Cl_2) and further purified by column chromatography (silica gel; eluent: *n*-hexane/CH_2Cl_2 (2:1 v/v); $R_f \approx 0.49$) to yield the product as orange powder (0.348 g, 59%). Elemental analysis: Found C, 81.00; H 4.58. $C_{26}H_{18}Fe$ requires C, 80.85; H 4.70%. ^{1}H-NMR (600.15 MHz, $CDCl_3$): $\delta_H = 8.29$ (s, 2H; Py-H), 8.17 (d, $J = 7.6$ Hz, 2H; Py-H), 8.07 (s, 4H; Py-H), 7.98 (t, $J = 7.6$ Hz, 1H; Py-H), 4.96 (pseudo-t, $J = 1.8$ Hz, 2H; Cp-H), 4.45 (pseudo-t, $J = 1.8$Hz, 2H; Cp-H), 4.08 (s, 5H; Cp-H) ppm. ^{13}C-NMR (150.9 MHz, $CDCl_3$): $\delta_C = 137.44$ (1C), 131.40 (2C), 131.05 (2C), 127.79 (2C), 127.41 (2C), 125.72 (1C), 125.20 (2C), 124.94 (1C), 123.55 (1C), 122.70 (2C), 85.61 (1C), 69.88 (5C), 69.48 (2C), 67.15 (2C) ppm. HRMS (MALDI): *m*/*z* calcd. for $C_{26}H_{18}Fe$ $[M]^+$ 386.0758, found 386.0758.

Synthesis of 1,1'-bis(2-pyrenyl)ferrocene ***2***

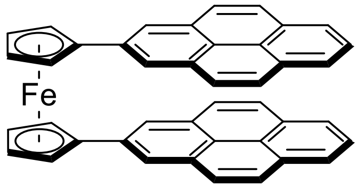

2-(Bpin)pyrene (0.475 g, 1.45 mmol, 3 equiv.), $PdCl_2$(dtbpf) (0.0157 g, 0.024 mmol, 0.05 eq.) and K_3PO_4 (0.614 g, 2.89 mmol, 6 eq.) were transferred into a dry Schlenk flask under a stream of Argon. Anhydrous DMF (14 mL) was then added. In a separate Schlenk flask 1,1'-diiodoferrocene (0.211 g, 0.48 mmol, 1 eq.) was dissolved in anhydrous DMF (10 mL), degassed by freeze-pump-thaw cycles, and cannulated to the main flask. The reaction mixture was stirred under Ar for 48 h at 60 °C. Water and CH_2Cl_2 were added to the cooled reaction mixture. The combined organic phase was washed with water/brine, dried over $MgSO_4$ and the solvent removed under vacuum. The remaining brown solid was purified by a silica plug (silica gel; eluent: CH_2Cl_2) and recrystallized from CH_2Cl_2/*n*-hexane. The product was received as red crystalline solid (144 mg, 51%). (Note: The solubility is decent for the raw product mixture but very low for the purified product). Elemental analysis: Found C, 85.97; H, 4.42. $C_{42}H_{26}Fe$ requires C, 86.01; H, 4.47%. ^{1}H-NMR (600.15 MHz, $CDCl_3$): $\delta_H = 7.76$ (dd, $J = 8.4, 6.4$ Hz, 2H; Py-H), 7.72 (d, $J = 6.9$ Hz, 4H; Py-H), 7.53 (s, 4H; Py-H), 7.37 (d, $J = 8.8$ Hz, 4H; Py-H), 7.30 (d, $J = 8.8$ Hz, 4H; Py-H), 4.89 (pseudo-t, $J = 1.8$ Hz, 4H; Cp-H), 4.49 (pseudo-t, $J = 1.8$ Hz, 4H; Cp-H) ppm. ^{13}C-NMR (150.9 MHz, $CDCl_3$): $\delta_C = 130.72$ (4C), 130.43 (4C), 126.75 (4C), 126.28 (4C), 125.03 (2C), 124.59 (4C), 121.69 (4C), 70.04 (4C), 67.72 (4C) ppm (not all peaks observed due to low solubility). HRMS (MALDI): *m*/*z* calcd. for $C_{42}H_{26}Fe$ $[M]^+$ 586.1384, found 586.1394.

*Synthesis of triangle **3***

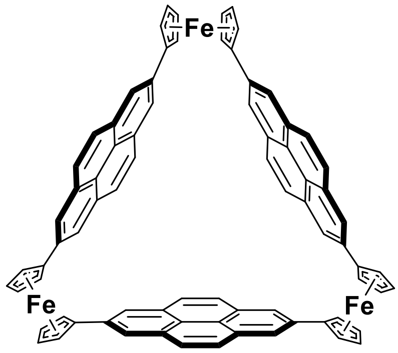

2,7-bis(Bpin)pyrene (1.000 g, 2.2 mmol, 1.1 eq.), $PdCl_2$(dtbpf) (0.1305 g, 0.2 mmol, 0.1 eq.) and K_3PO_4 (1.6996 g, 8.0 mmol, 4 eq.) were added to a dry Schlenk flask under a stream of Ar. 1,1'-Diiodoferrocene (0.8764 g, 2.0 mmol, 1 eq.) was dissolved in anhydrous DMF (100 mL) and cannulated to the reaction mixture. After stirring under Ar at 80 °C for 16 h, more catalyst $PdCl_2$(dtbpf) (0.0653 g, 0.1 mmol, 0.05 eq.) in 10 mL DMF was added. The reaction was continued at 80 °C for 48 h. The resulting brownish suspension was diluted with water and CH_2Cl_2, sonicated for 10 min, and filtered. The filter cake was washed with water and CH_2Cl_2. Gradient sublimation of the insoluble filter cake as described in ref. 3 provided **cyclophane** (Chart 1) as red crystalline solid in <1% yield.[3] The phases of the combined filtrates were separated, and the organic phase washed with water/brine and dried over $MgSO_4$. The solvent was evaporated under reduced pressure and the resulting brown solid dissolved in CH_2Cl_2 and subjected to a short silica column (silica gel; eluent: CH_2Cl_2). The raw product was further purified by column chromatography (silica gel; eluent: *n*-hexane/CH_2Cl_2 (1:2 v/v); $R_f \approx 0.67$) to remove acyclic side products (see Figs. S12,13). After precipitation from CH_2Cl_2/*n*-hexane the product was received as fine orange powder (0.048 g, 6%). ^{1}H-NMR (600.15 MHz, $CDCl_3$): $\delta_H = 7.98$ (s, 12H; Py-H), 7.75 (s, 12H; Py-H), 4.61–4.59 (m, 24H; Cp-H) ppm. ^{13}C-NMR (150.9 MHz, $CDCl_3$): $\delta_C = 136.59$ (6C), 131.12 (12C), 128.02 (12C), 123.78 (6C), 123.04 (12C), 86.94 (6C), 70.20 (12C), 69.62 (12C) ppm. HRMS (MALDI): *m*/*z* calcd. for $C_{78}H_{48}Fe_3$ $[M]^+$ 1152.1804, found 1152.1807.

Nuclear Magnetic Resonance (NMR) spectra

^{1}H-NMR spectrum of 2-ferrocenylpyrene ***1***

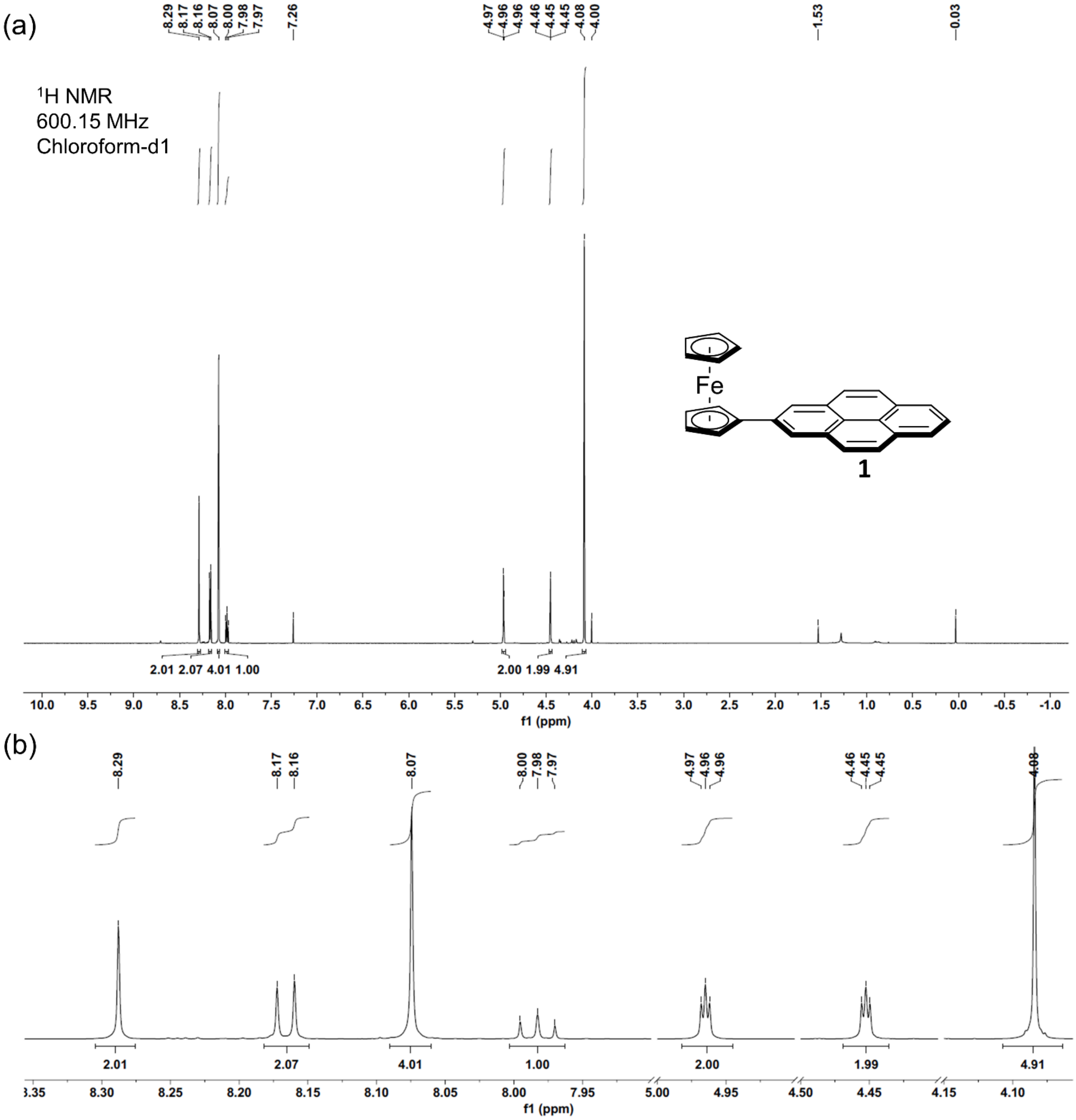

Fig. S1 ^{1}H-NMR (600.15 MHz) spectra of **1** measured in chloroform-d1 showing full peak range (a) and signals only related to **1** (b).

*^{13}C-NMR spectrum of 2-ferrocenylpyrene **1***

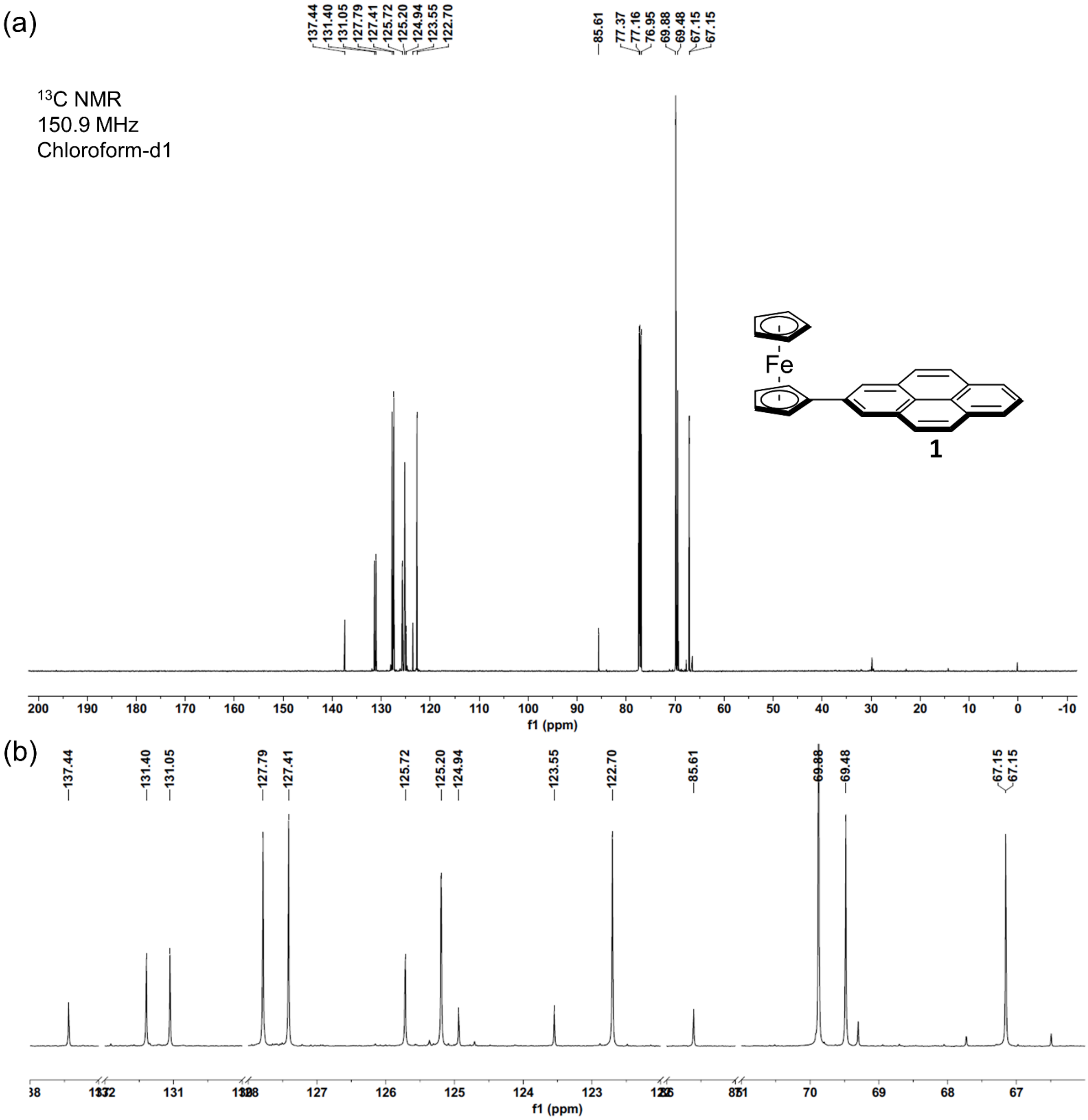

Fig. S2 ^{13}C-NMR (150.9 MHz) spectra of **1** measured in chloroform-d1 showing full peak range (a) and signals only related to **1** (b).

^{1}H-NMR spectrum of 1,1'-bis(2-pyrenyl)ferrocene ***2***

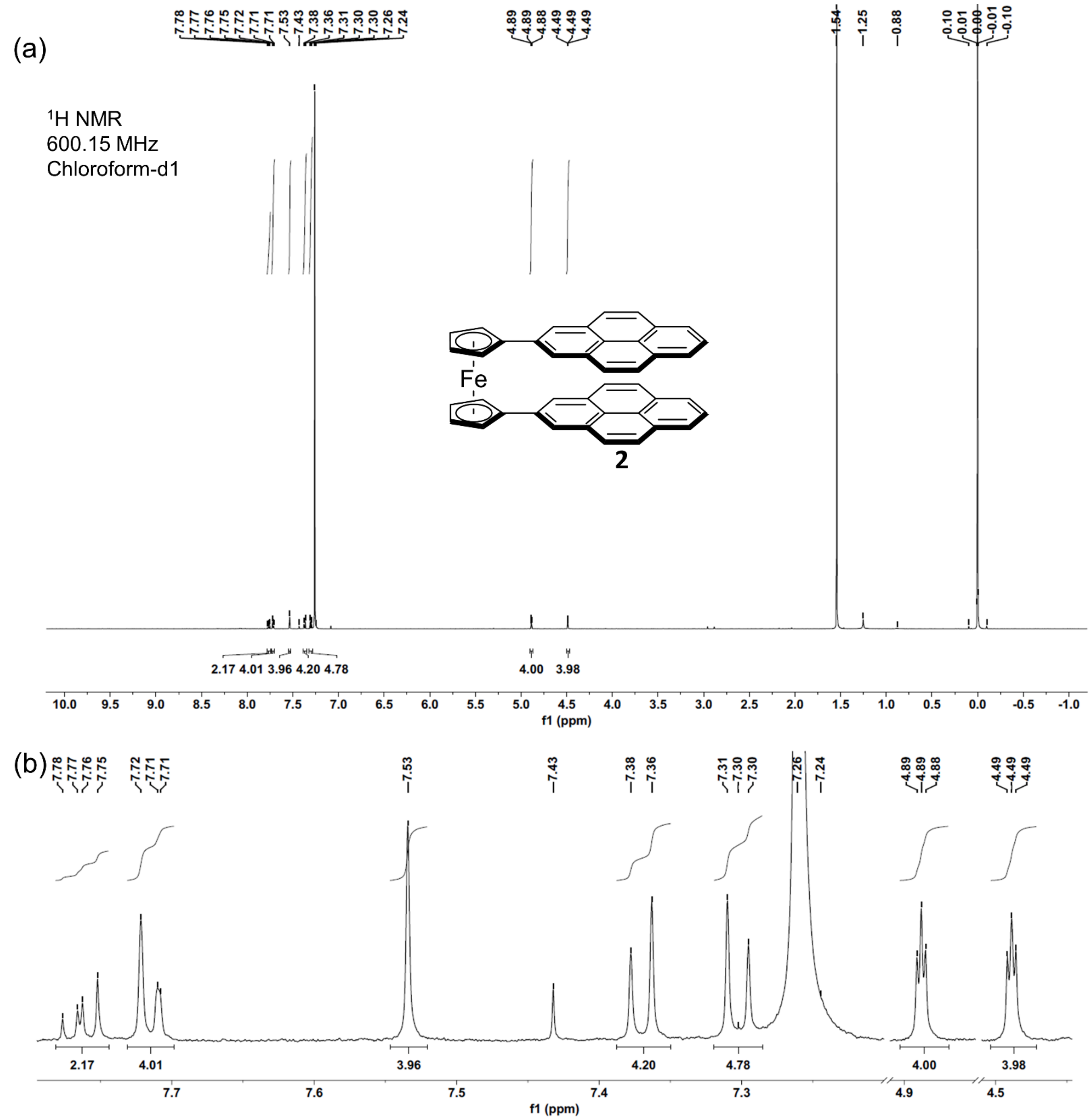

Fig. S3 ^{1}H-NMR (600.15 MHz) spectra of **2** measured in chloroform-d1 showing full peak range (a) and signals only related to **2** (b).

^{13}C-NMR spectrum of 1,1'-bis(2-pyrenyl)ferrocene ***2***

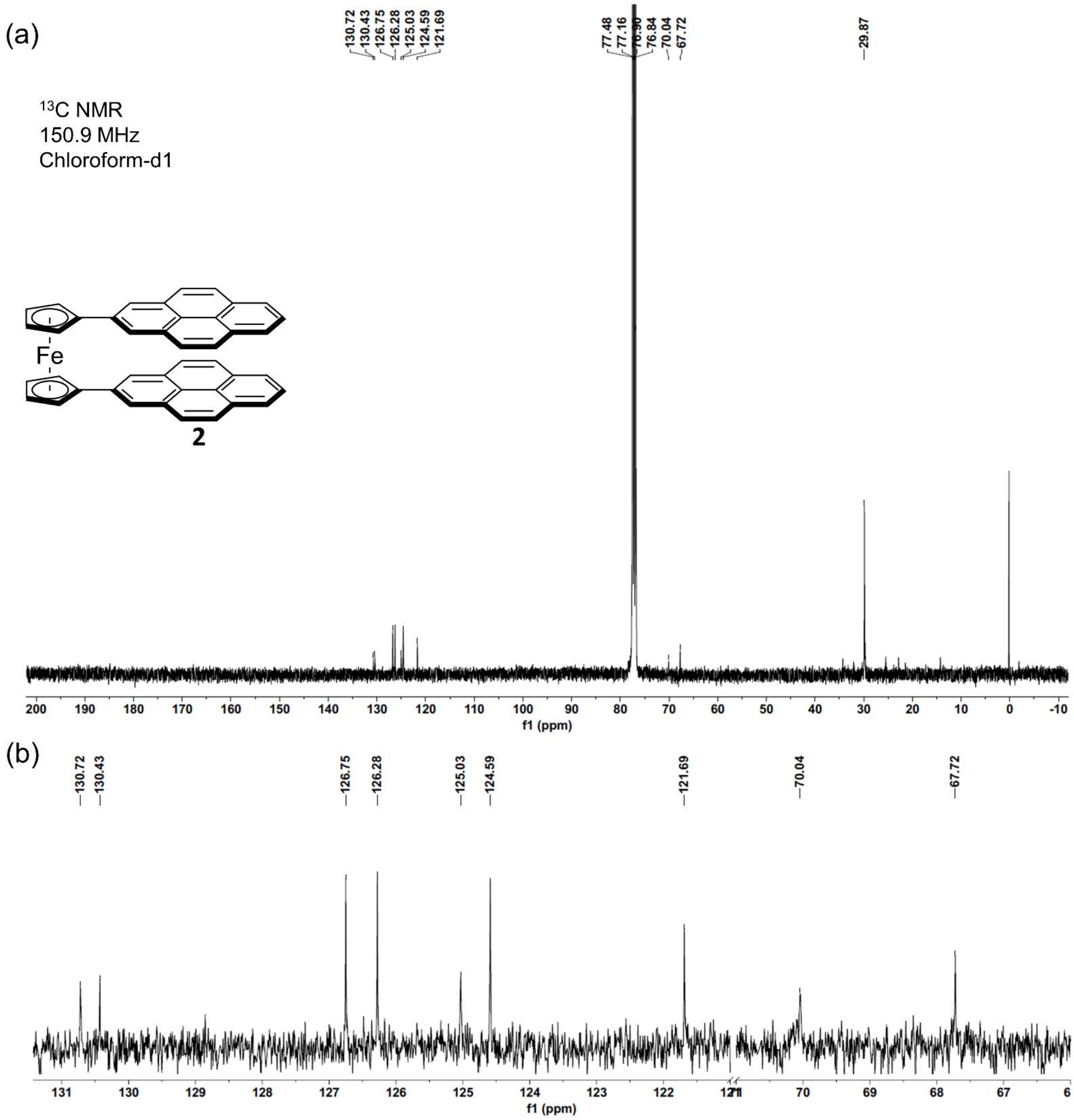

Fig. S4 ^{13}C-NMR (150.9 MHz) spectra of **2** measured in chloroform-d1 showing full peak range (a) and signals only related to **2** (b).

^{1}H-NMR spectra of triangle ***3***

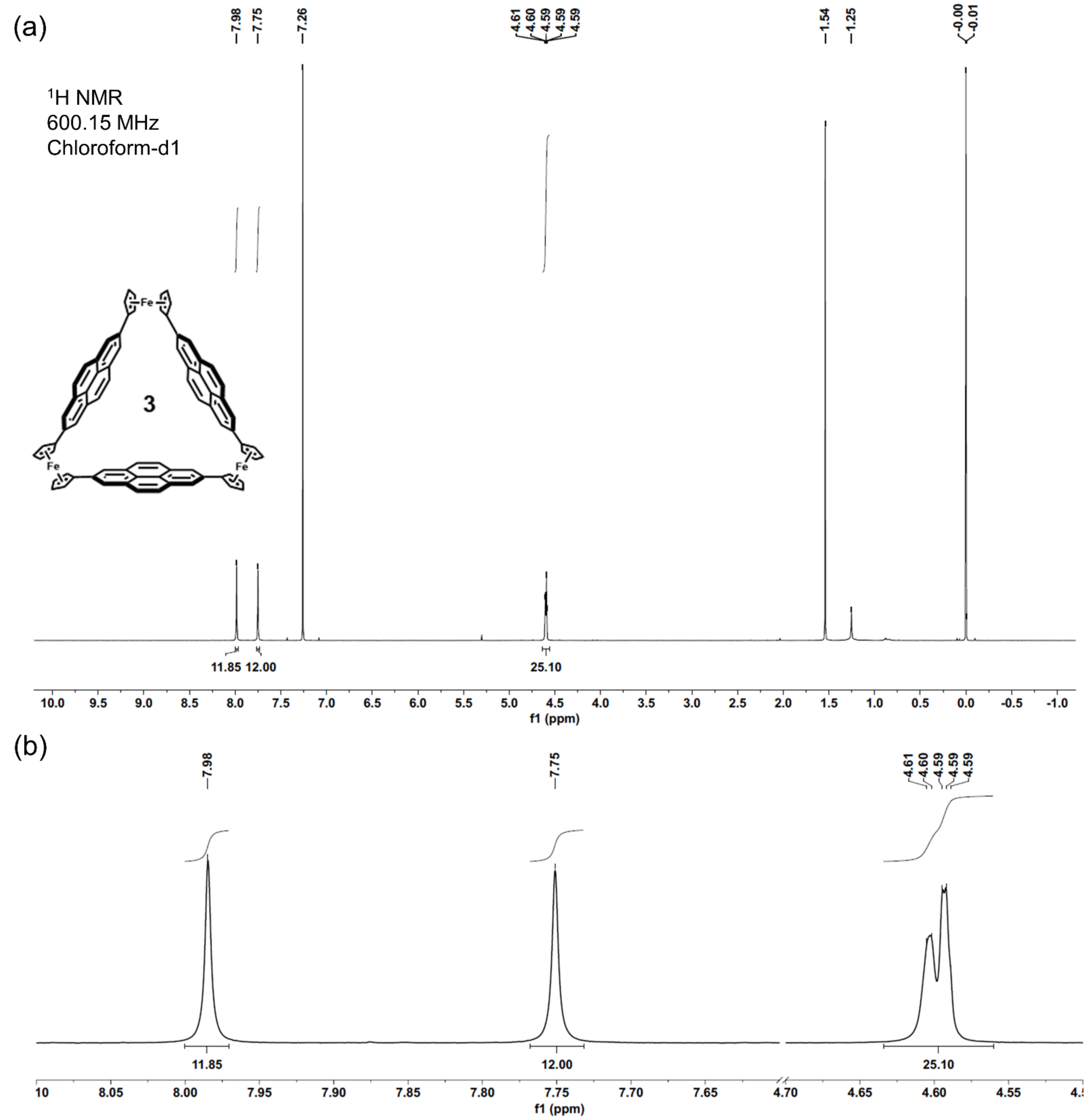

Fig. S5 ^{1}H-NMR (600.15 MHz) spectra of **3** measured in chloroform-d1 showing full peak range (a) and signals only related to **3** (b).

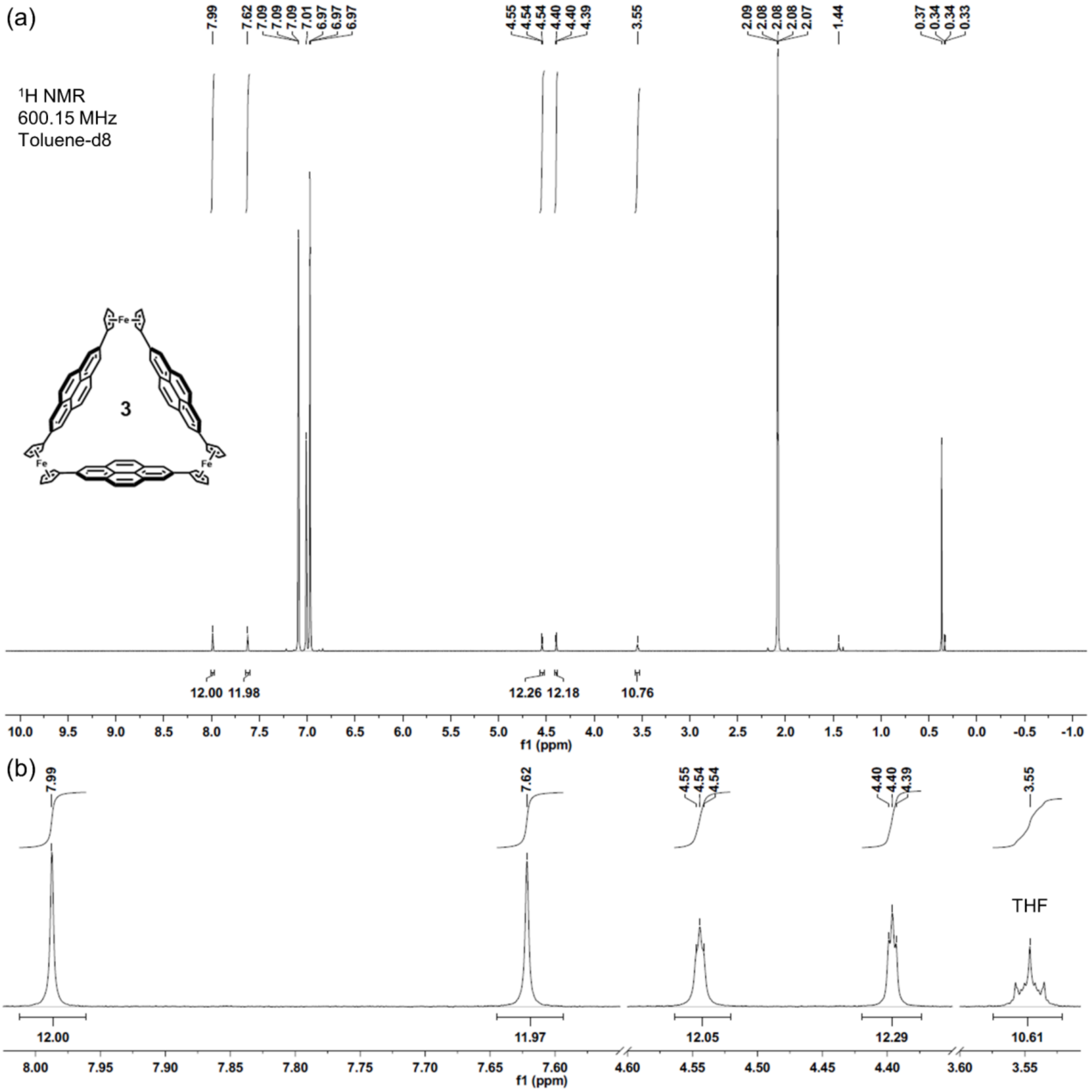

Fig. S6 ^{1}H-NMR (600.15 MHz) spectra of **3·5THF** measured in toluene-d8 showing full peak range (a) and signals only related to **3·5THF** (b).

*^{13}C-NMR spectrum of triangle **3***

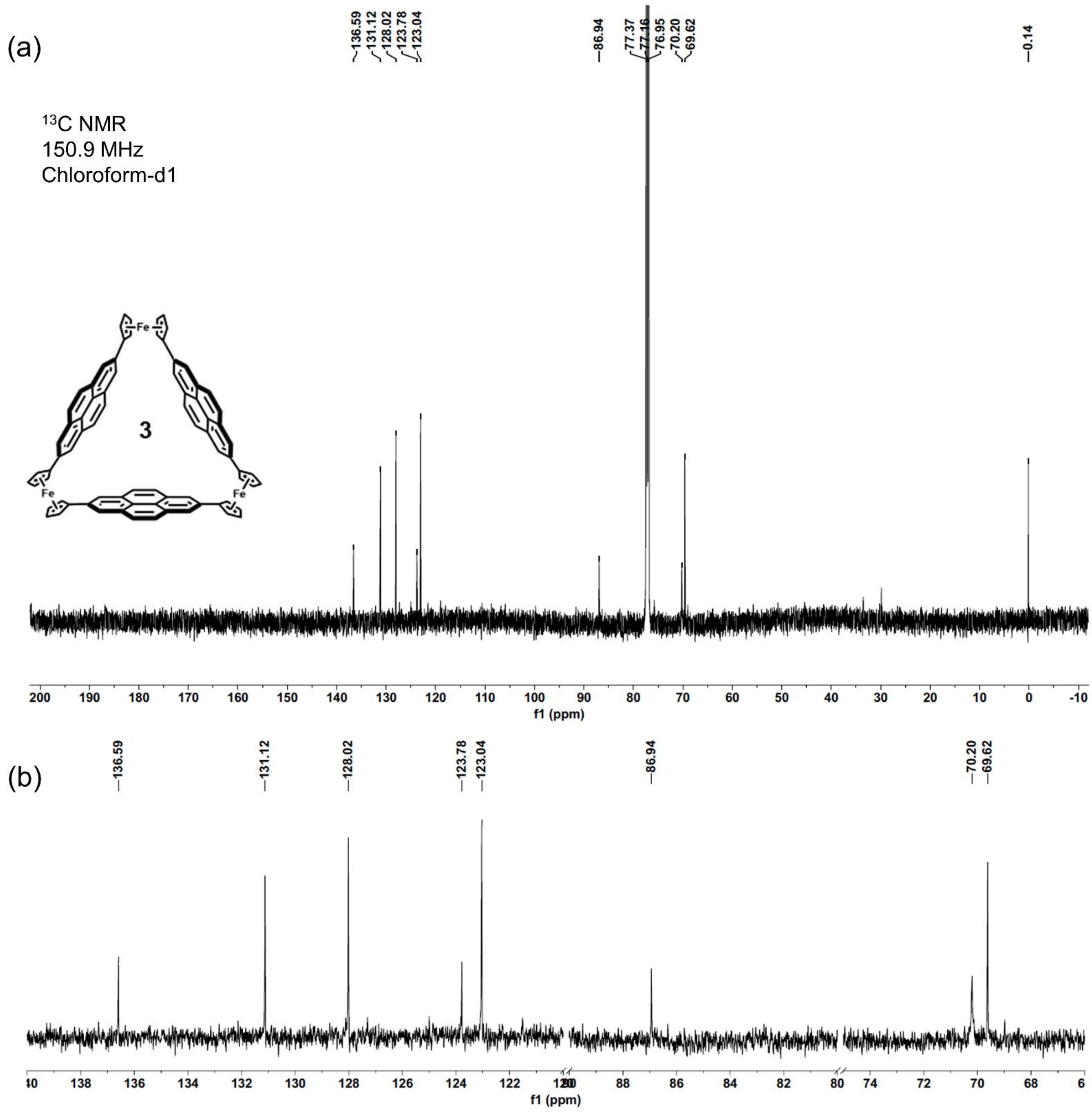

Fig. S7 ^{13}C-NMR (150.9 MHz) spectra of **3** measured in chloroform-d1 showing full peak range (a) and signals only related to **3** (b).

Matrix-assisted laser desorption/ionisation (MALDI) high-resolution mass spectrometry (HRMS) data

*MALDI mass spectrum of 2-pyrenylferrocene **1***

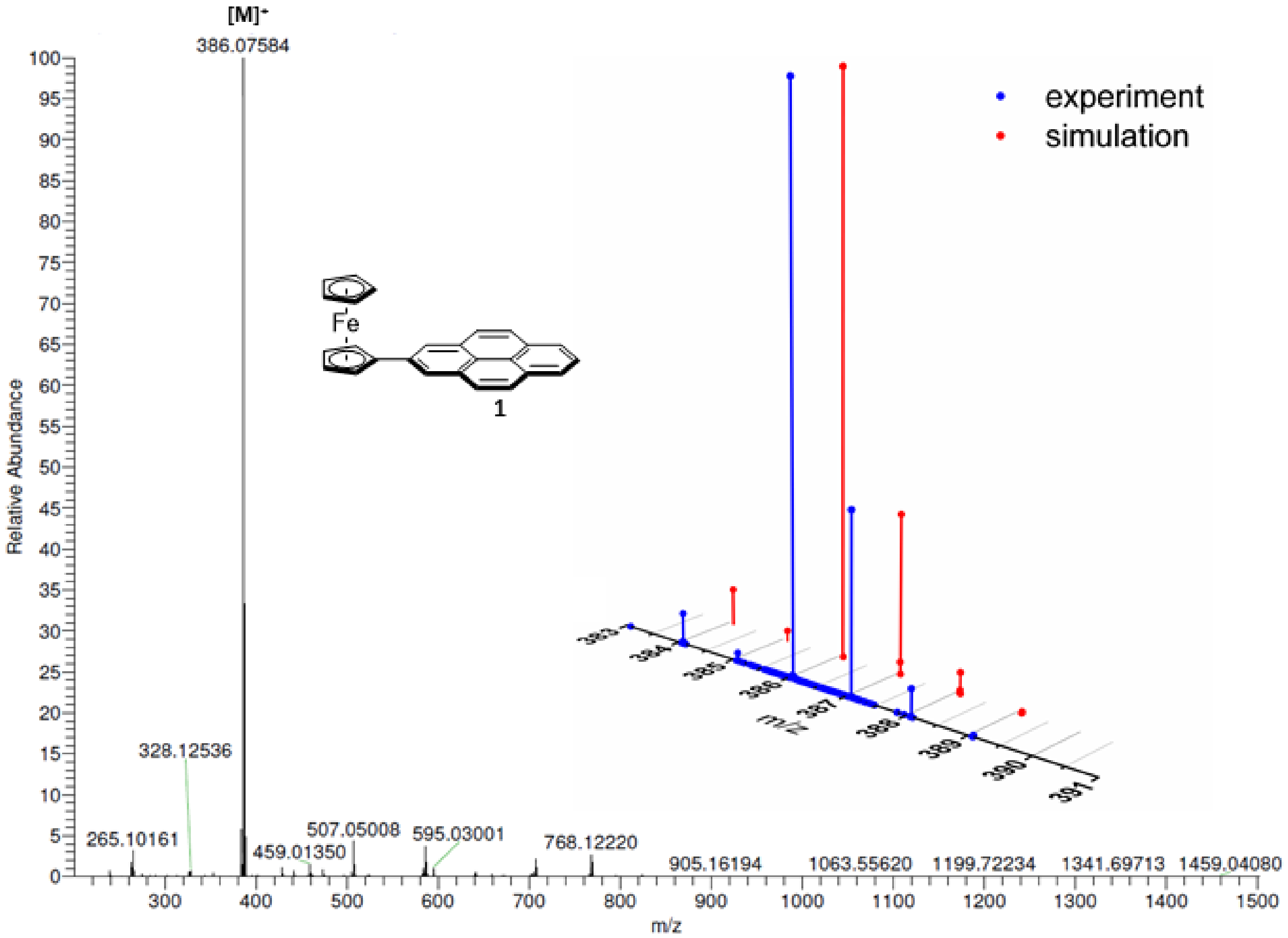

Fig. S8 Mass spectrum (MALDI) of **1**; calcd. (*m/z)* for $C_{26}H_{18}Fe$ $[M]^+$ 386.0758, found 386.07584; Inset: comparison of the simulated (red) to the experimental (blue) isotope distribution of **1**.

*MALDI mass spectrum of 1,1'-bis(2-pyrenyl)ferrocene **2***

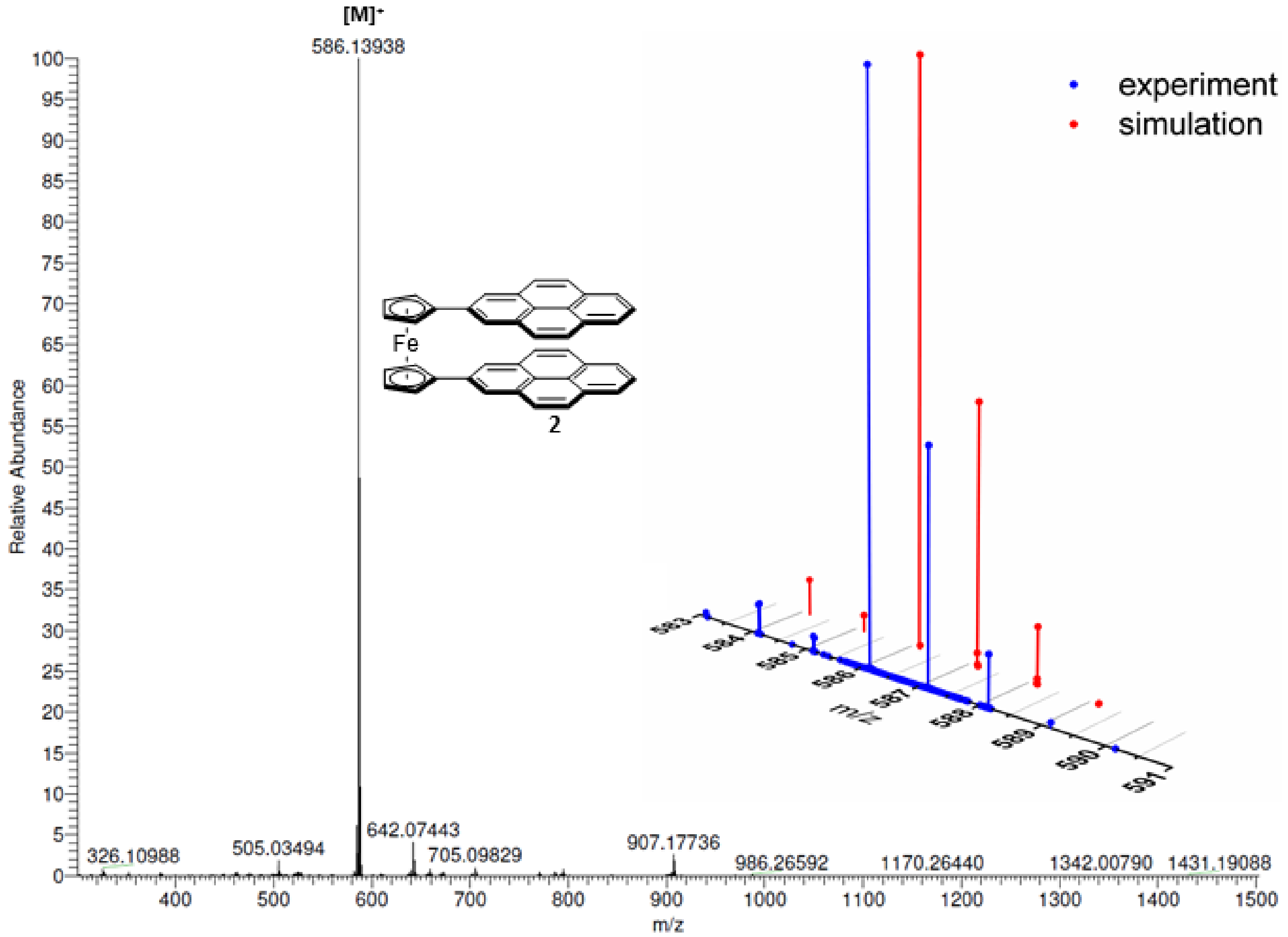

Fig. S9 Mass spectrum (MALDI) of **2**; calcd. (*m*/*z*) for $C_{42}H_{26}Fe$ [M]$^+$ 586.1384, found 586.13938; Inset: comparison of the simulated (red) to the experimental (blue) isotope distribution of **2**.

*MALDI mass spectrum of triangle **3***

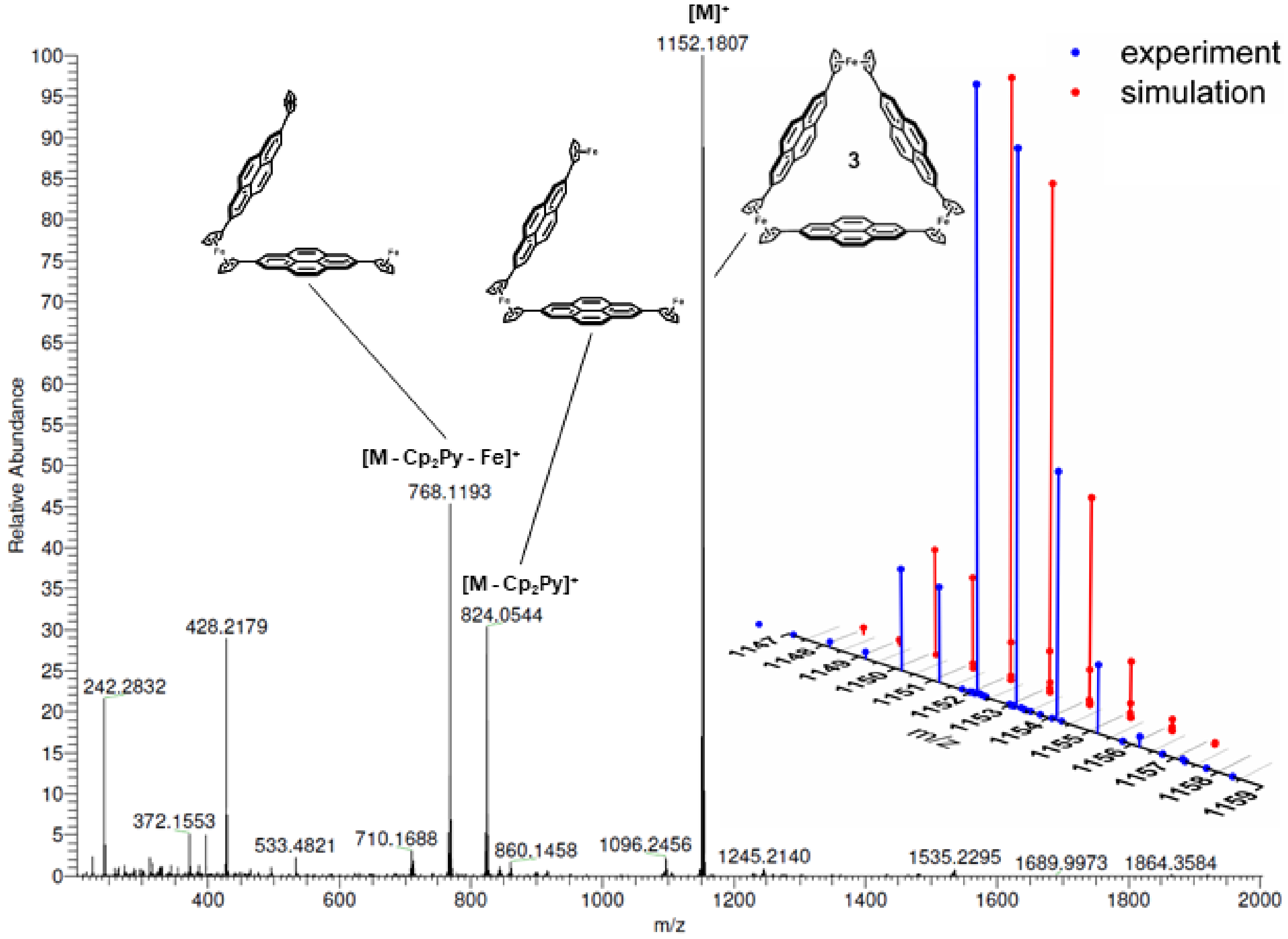

Fig. S10 Mass spectrum (MALDI) of **3** showing fragmentation by release of Cp-Py-Cp and FeCp-Py-Cp; calcd. (*m*/*z)* for $C_{78}H_{48}Fe_3$ $[M]^+$ 1152.1804, found 1152.1807; $[M - Cp_2Py]^+$ calcd. (*m*/*z*) 824.0552, found 824.0554; $[M - Cp_2Py - Fe]^+$ calcd. (*m*/*z*) 768.1203, found 768.1193; Inset: comparison of the simulated (red) to the experimental (blue) isotope distribution of **3**.

*Higher-energy collisional dissociation (HCD) mass spectrometry (MALDI) of triangle **3***

The MS data of triangle **3** (Fig. S10) reveal two additional peaks at *m*/*z* 824.0554 and 768.1193 that we attribute to a fragmentation of **3** by release of Cp-Py-Cp and FeCp-Py-Cp, respectively. The latter peak also coincides with the result we reported for **cyclophane** that can be isolated as a side product using the same reaction conditions employed here.[3]

To verify the fragmentation of triangle **3** (see Fig. S10) and to rule out contamination with **cyclophane** the higher-energy collisional dissociation (HCD) method has been applied as implemented in an Orbitrap LTQ XL mass spectrometer.[4] Ions with *m*/*z* 1152.179 ($[M]^+$) have been trapped in a collision cell and dissociated by collisions with N_2 gas. At lower collision energies only $[M]^+$ could be detected. At higher collision energies two additional signals appeared at *m*/*z* 824.0522 and 768.1170 that verify the described fragmentation into $[M - Cp_2Py]^+$ and $[M - Cp_2Py - Fe]^+$, respectively.

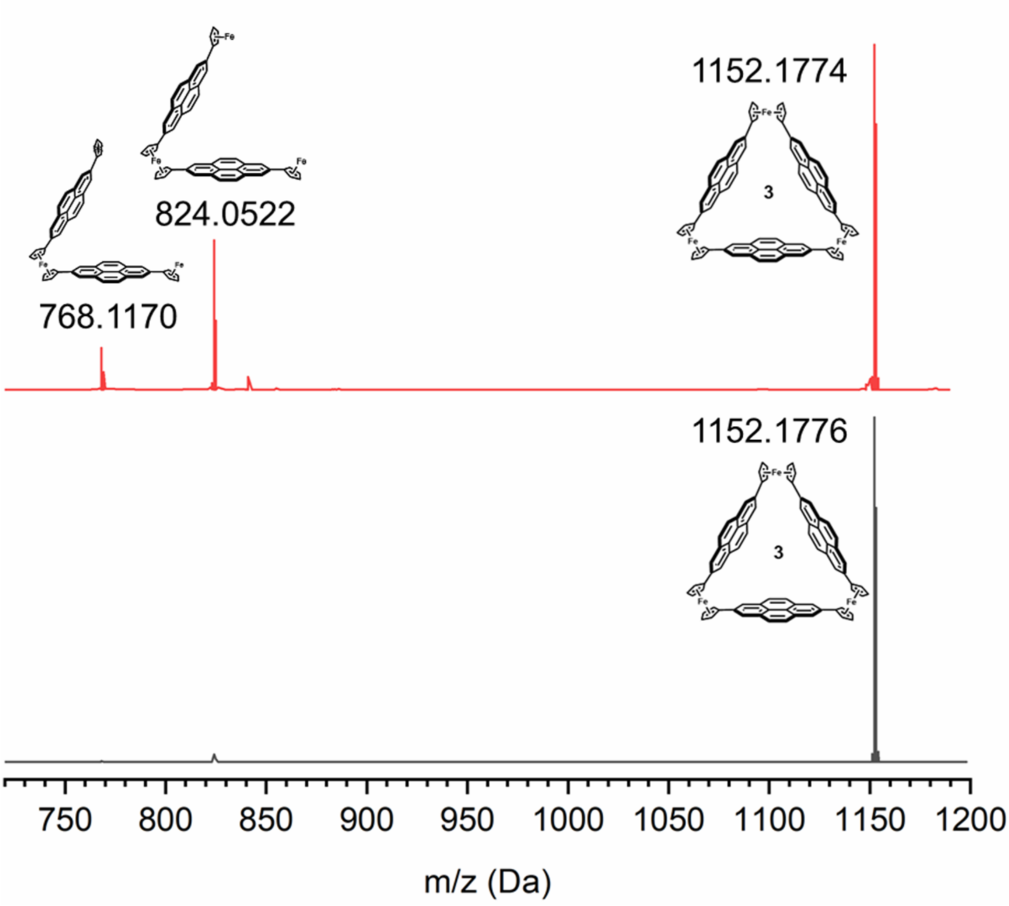

Fig. S11 Mass spectra (MALDI) of triangle **3** measured by applying the HCD method for the $[M]^+$ ion at *m*/*z* 1152.179 with lower (black) and higher (red) collision energies. At higher energies two additional peaks appear at *m*/*z* 768.1170 and 824.0522 that verify the fragmentation of **3** as indicated.

*MALDI mass spectra of crude product mixtures of **3** after different reaction times*

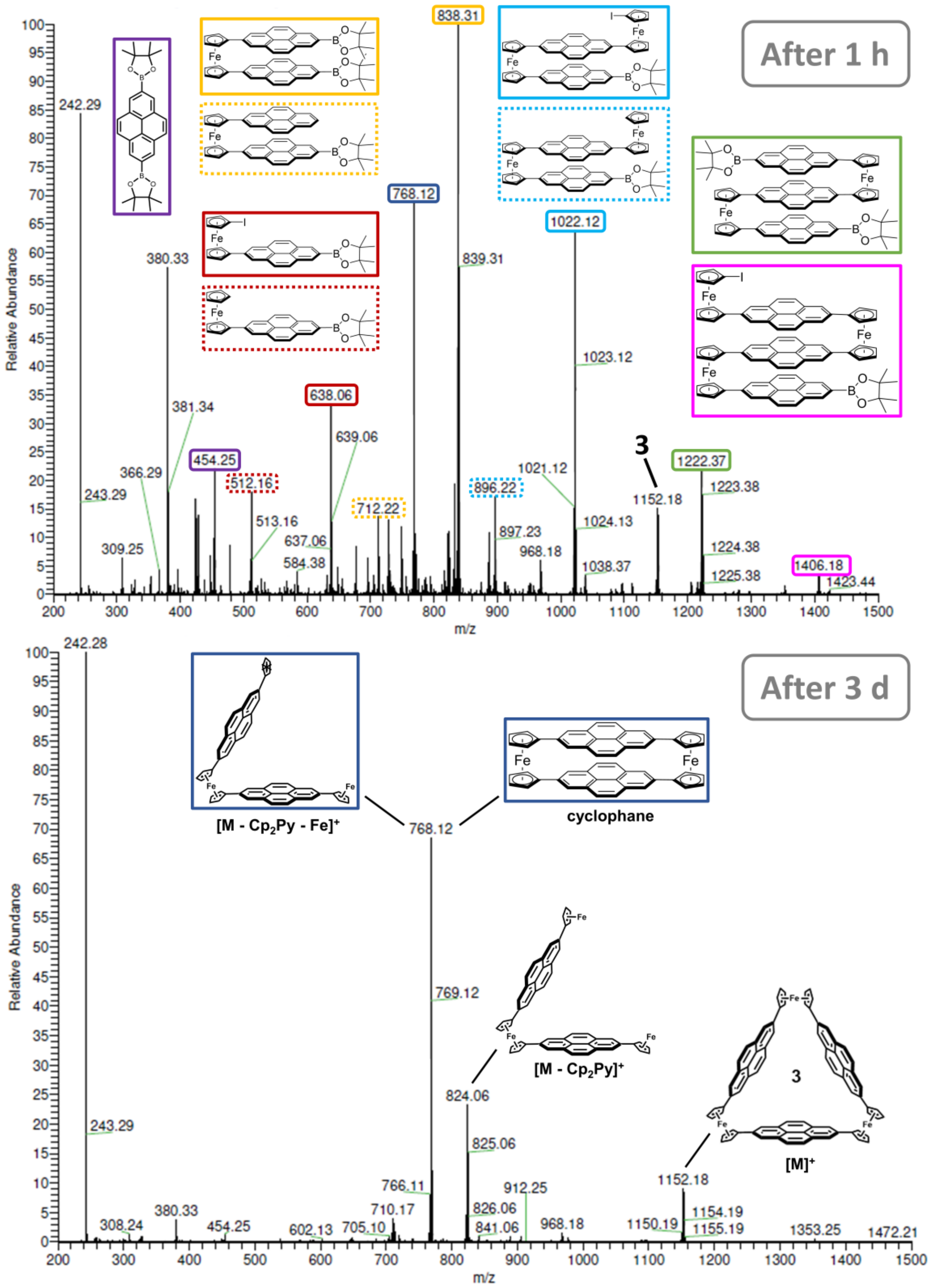

Fig. S12 Mass spectra (MALDI) of aliquots taken from the reaction mixture of triangle **3** after a reaction time of 1 h and 3 d; reaction conditions as described on page S5 with a 0.5 mM scale and a reaction temperature of 60 °C; work-up procedure was followed until completion of the short silica gel column (eluent: CH_2Cl_2). Reaction intermediates (solid lines) and side products (dashed lines) were assigned to their respective *m*/*z* peaks by coloured boxes. Note that insoluble (side) products may not be represented in these spectra.

*MALDI mass spectrum of side products that were recovered during purification of **3***

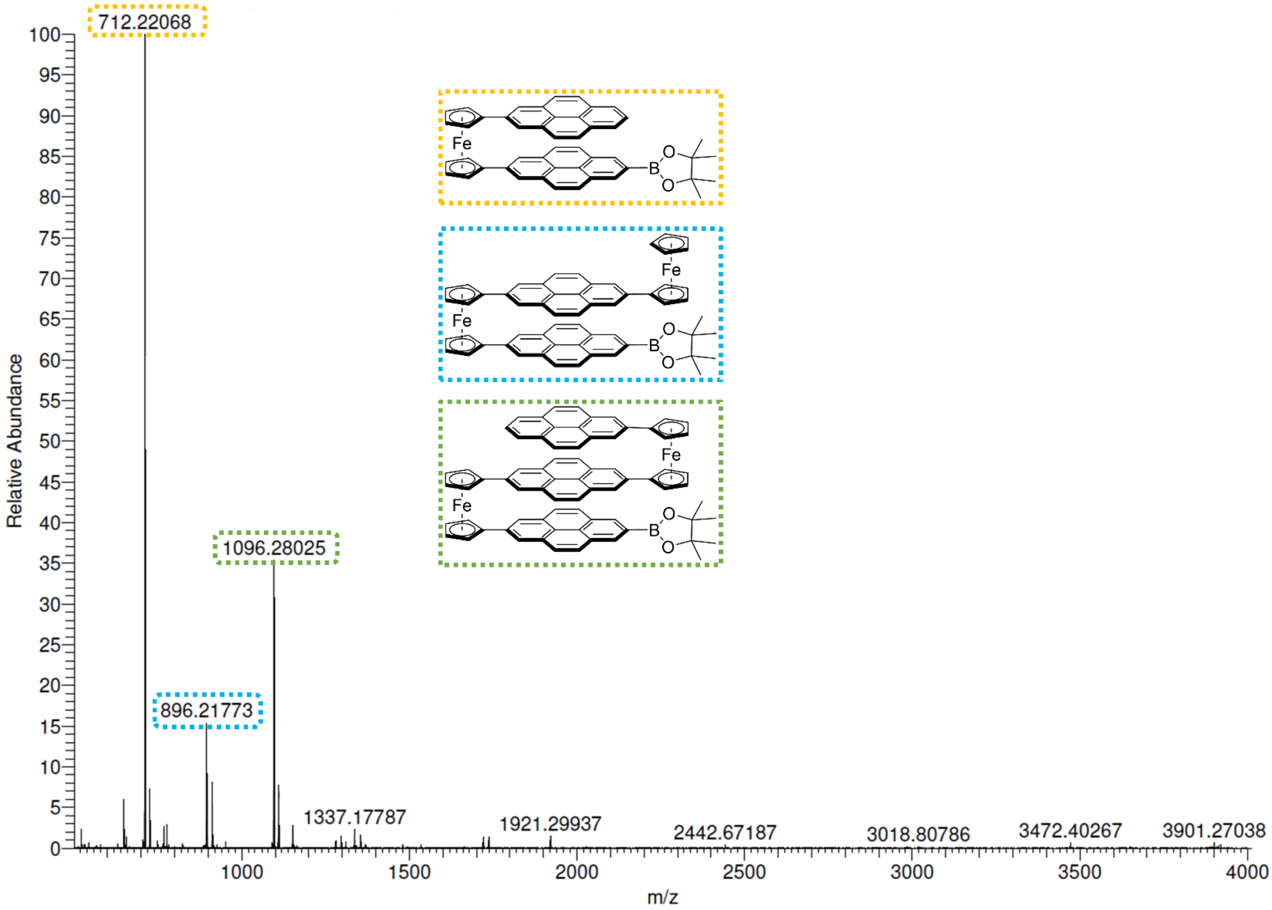

Fig. S13 Mass spectrum (MALDI) of a mixture of some side products that was recovered during chromatographic purification of triangle **3** as described on page S5. The side products were assigned to their respective *m*/*z* peaks by coloured boxes and likely produced *via* dehalogenation (blue) or deborylation (green, yellow) of reaction intermediates (see Fig. S12).

Variable-Temperature NMR measurements of triangle **3**

*^{1}H-NMR spectra of **3** recorded at variable temperatures (400 MHz)*

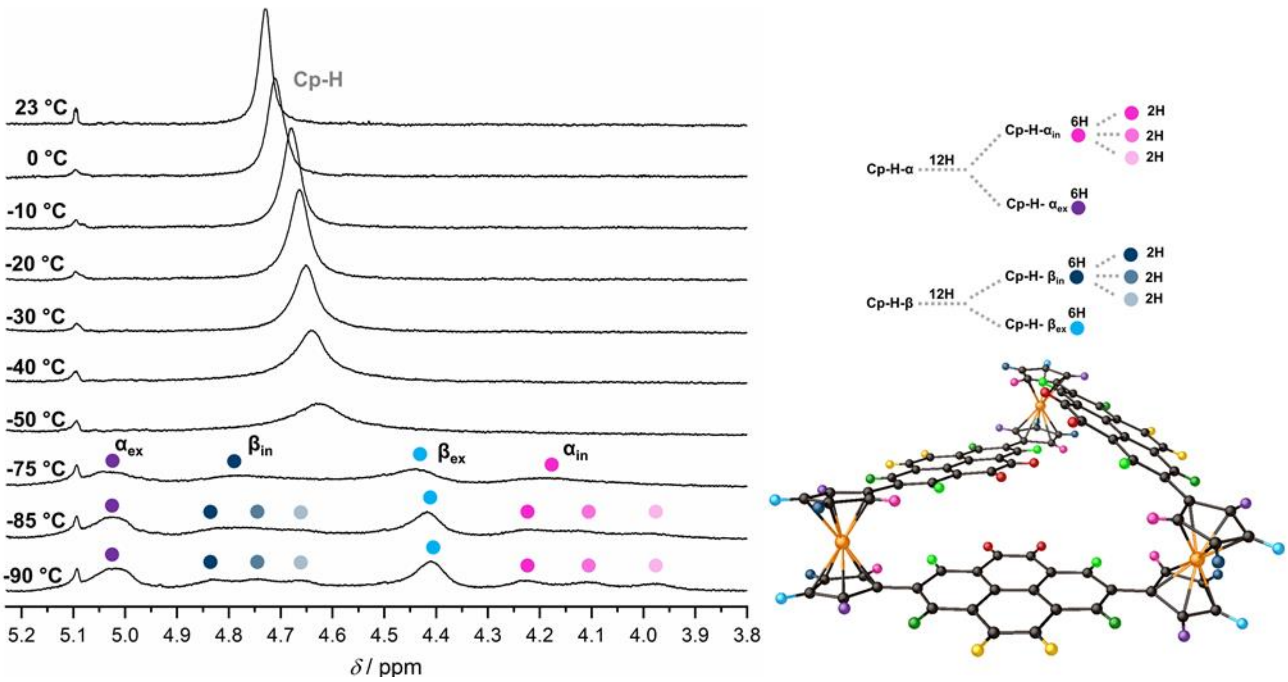

Fig. S14 Cp-H region of ^{1}H-NMR (CD_2Cl_2, 400MHz) spectra of **3** (left) measured at variable temperatures. Peaks are assigned tentatively by coloured cycles and protons are coloured accordingly in the crystal structure (lower right). The splitting patterns of the peaks are shown in the upper right image.

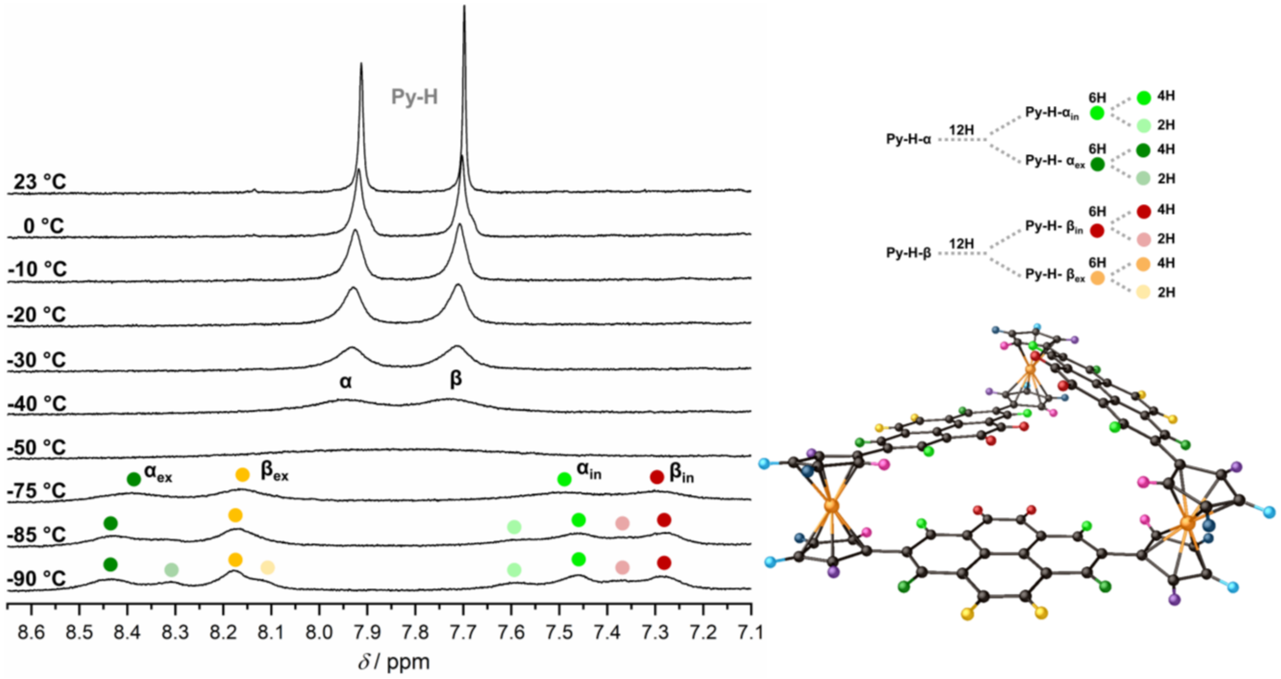

Fig. S15 Py-H region of ^{1}H-NMR (CD_2Cl_2, 400MHz) spectra of **3** (left) measured at variable temperatures. Peaks are assigned tentatively by coloured cycles and protons are coloured accordingly in the crystal structure (lower right). The splitting patterns of the peaks are shown in the upper right image.

^{1}*H-NMR spectra of* ***3*** *recorded at variable temperatures (800 MHz)*

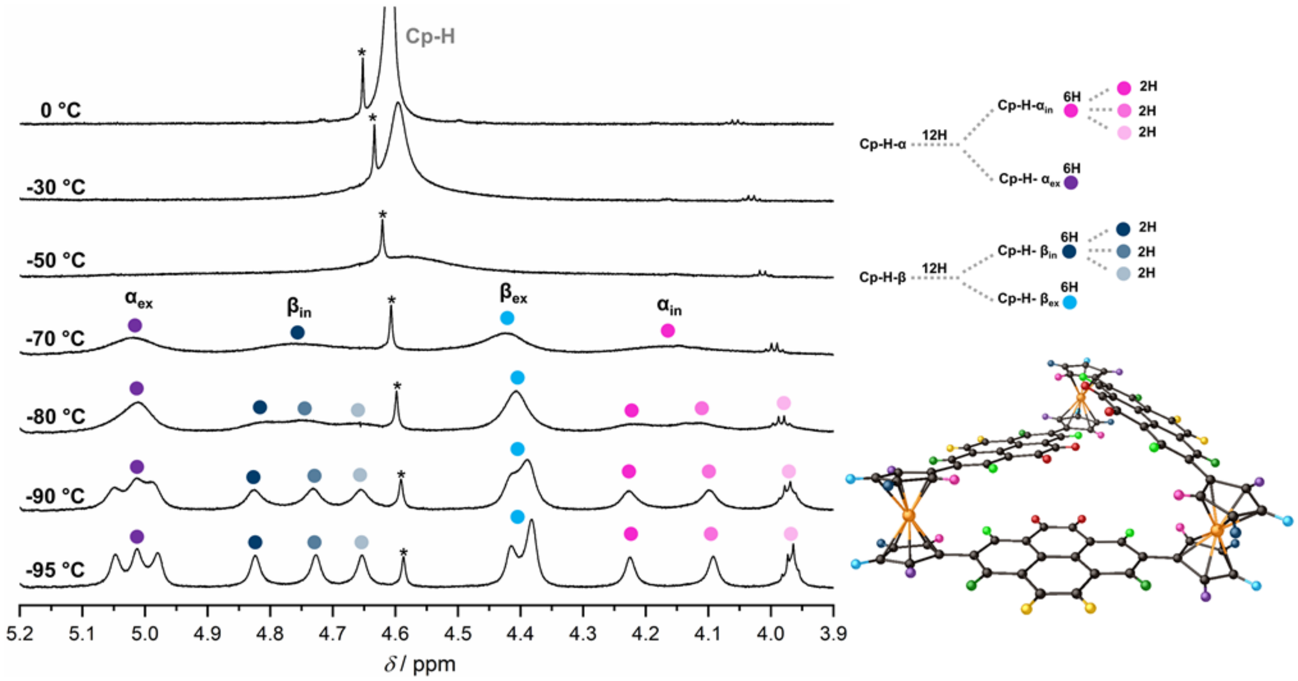

Fig. S16 Cp-H region of ^{1}H-NMR (CD_2Cl_2, 800MHz) spectra of **3** (left) measured at variable temperatures. Peaks are assigned tentatively by coloured cycles and protons are coloured accordingly in the crystal structure (lower right). The splitting patterns of the peaks are shown in the upper right image. * marks peaks that correspond to an impurity introduced by extended experiments in pentane and toluene.

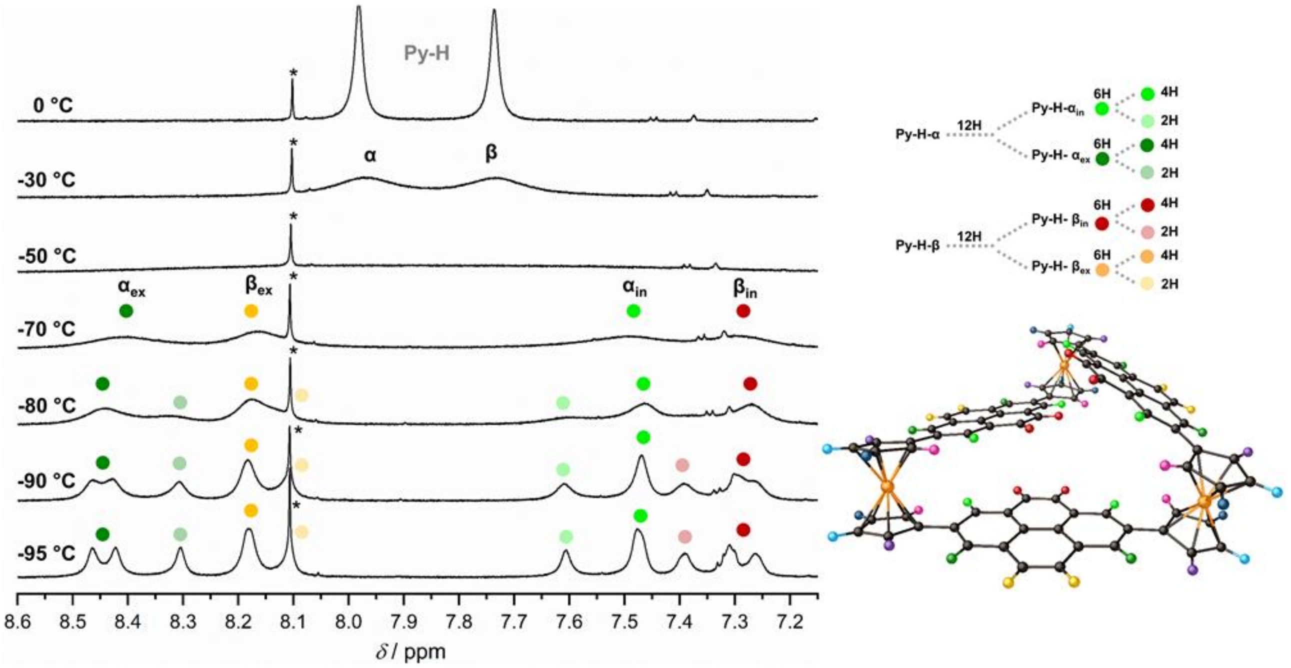

Fig. S17 Py-H region of ^{1}H-NMR (CD_2Cl_2, 800MHz) spectra of **3** (left) measured at variable temperatures. Peaks are assigned tentatively by coloured cycles and protons are coloured accordingly in the crystal structure (lower right). The splitting patterns of the peaks are shown in the upper right image. * marks peaks that correspond to an impurity introduced by extended experiments in pentane and toluene.

*Low-temperature ROESY 2D-NMR spectrum of **3***

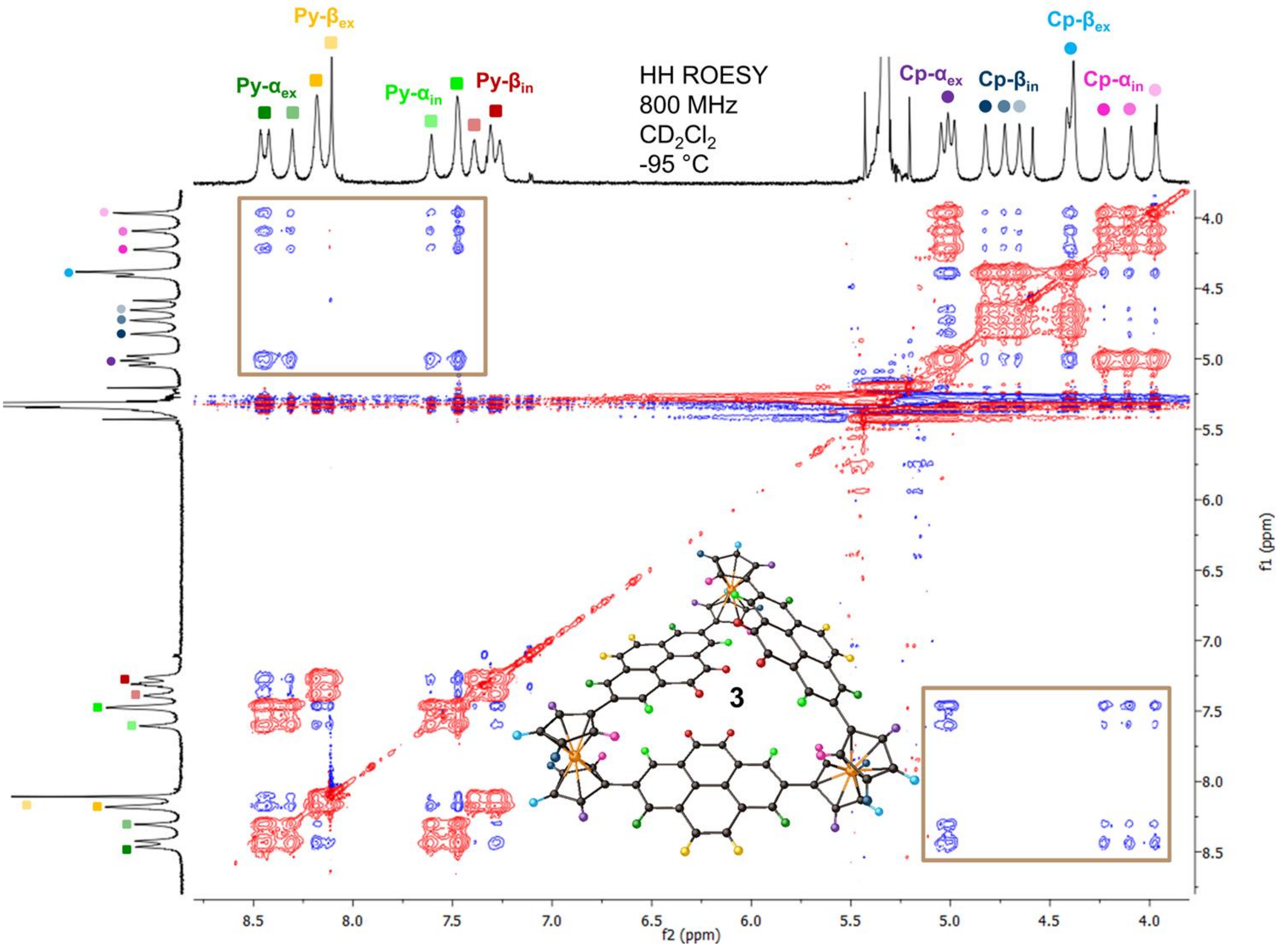

Fig. S18 2D ROESY NMR spectrum of triangle **3** measured at $T = -95$ °C with 450 ms ROESY spinlock time. Peaks are tentatively assigned with coloured circles for Cp and squares for Py protons. The brown boxes mark through-space interaction between Py-α and Cp-α protons. Inset: Crystal structure of **3** with protons coloured according to the presented peak assignment.

Low-temperature TOCSY 2D-NMR spectrum of ***3***

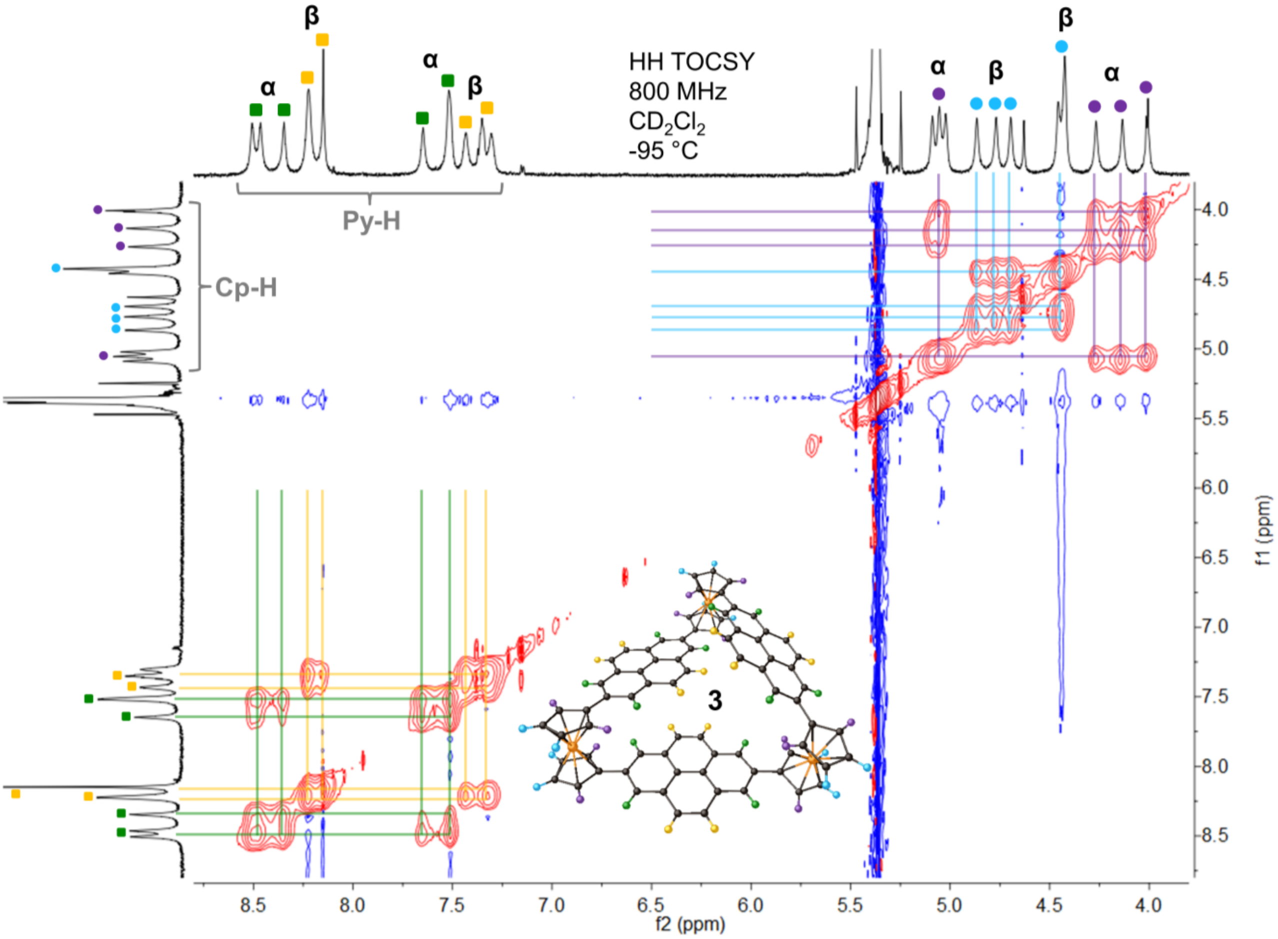

Fig. S19 2D TOCSY NMR spectrum of triangle **3** measured at $T = -95$ °C with 30 ms TOCSY spinlock time. Peaks are tentatively assigned with coloured circles for Cp and squares for Py protons and cross peaks are connected by correspondingly coloured lines. Inset: Crystal structure of **3** with protons coloured according to the presented peak assignment.

*Full ^{1}H-NMR spectra of **3** recorded at variable temperatures (400 MHz)*

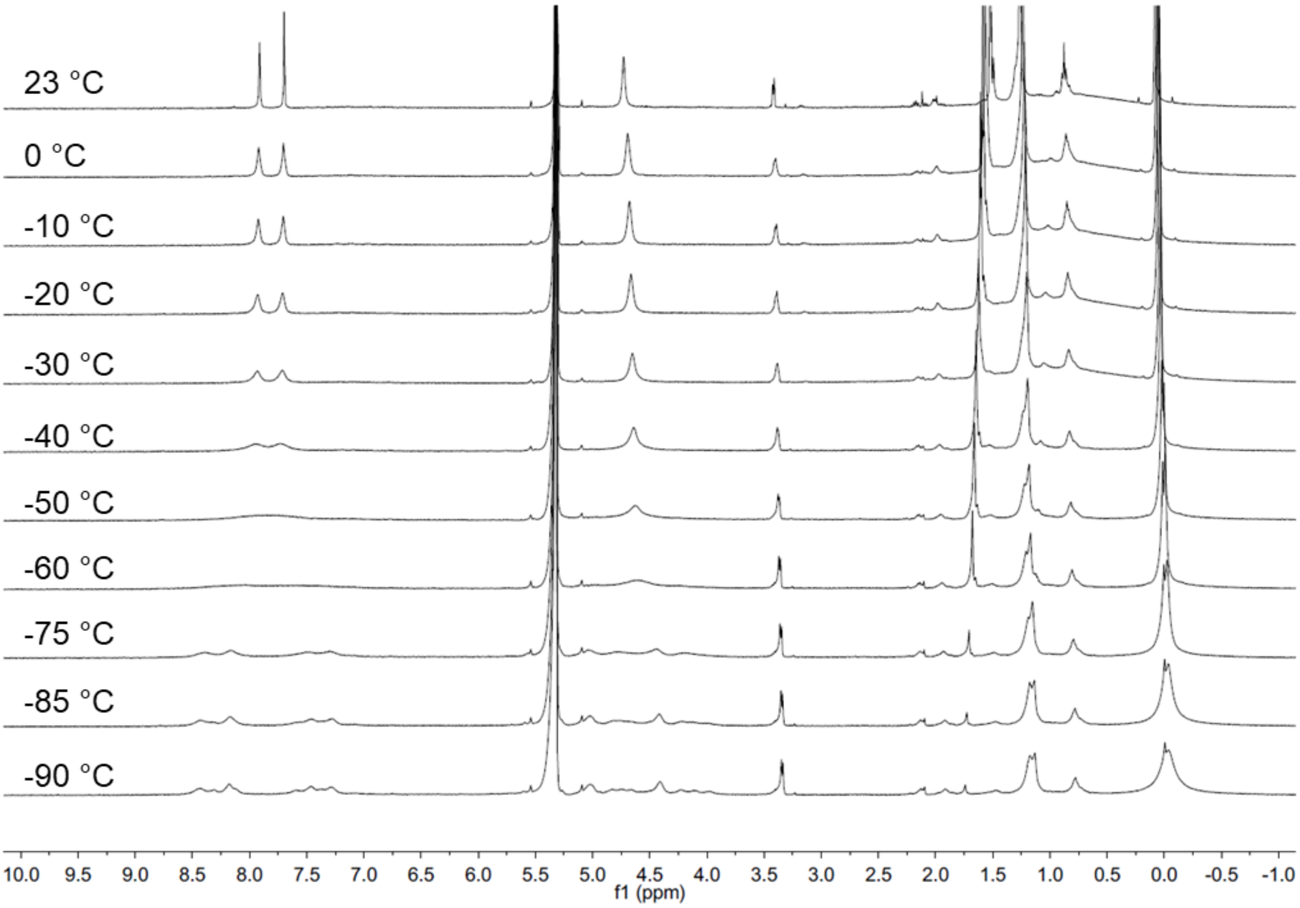

Fig. S20 Full range of ^{1}H-NMR (CD_2Cl_2, 400MHz) spectra of **3** measured at variable temperatures as indicated at each spectrum.

*Full ^{1}H-NMR spectra of **3** recorded at variable temperatures (800 MHz)*

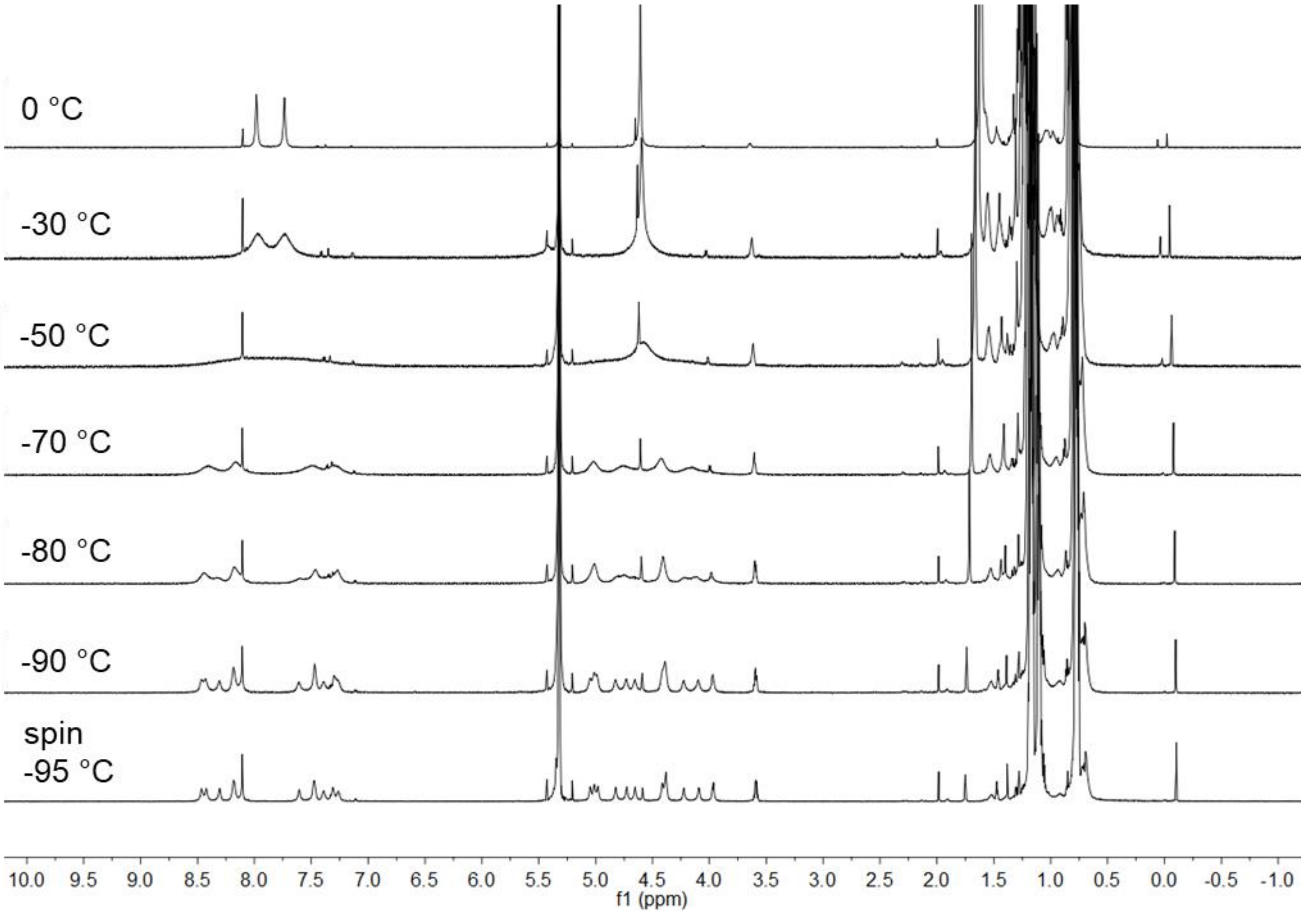

Fig. S21 Full range of ^{1}H-NMR (CD_2Cl_2, 800MHz) spectra of **3** measured at variable temperatures as indicated at each spectrum. Note that at *T* = –95 °C tube spin was turned on.

Electrochemistry

Cyclic and square-wave voltammetries (CV and SWV) have been performed on a Biologic SP-150 potentiostat, operated using EC-Lab software V11.12. The commercial electrolytes Na[BArF$_{24}$] and [NBu$_4$][PF$_6$] were purified by recrystallisation. [NBu$_4$][BArF$_{24}$] was synthesised and purified as previously reported.[5,6] All electrolytes were stored and handled in an Ar glovebox. The solvent CH_2Cl_2 was dried by a solvent purification system (MBraun) and stored over a molecular sieve. Prior to electrochemical experiments the electrolyte/solvent mixture was purged with Ar for at least 5 min. The electrochemical setup consisted of a one-compartment cell fitted with a glassy carbon working electrode (disk, 3.0 mm), Pt counter electrode and Pt pseudo reference electrode. The shown data are corrected for ohmic drop (PEIS method) and reported *vs.* [Cp$_2$Fe]/[Cp$_2$Fe]$^+$ (Fc/Fc$^+$) with corrections of –0.55 V for [NBu$_4$][PF$_6$]/CH_2Cl_2 and –0.62 V for [NBu$_4$][BArF$_{24}$]/CH_2Cl_2 against the internal standard [Cp*$_2$Fe]/[Cp*$_2$Fe]$^+$.[7,8] The analyte concentrations ranged from 0.1–1 mM and was very low for **2** due to limited solubility. If not stated otherwise, the second cycle of a CV experiment is plotted with all consecutive cycles being identical. Sweeping direction for all experiments is from negative to positive potentials.

*Cyclic Voltammograms of **1**, **2** and **3***

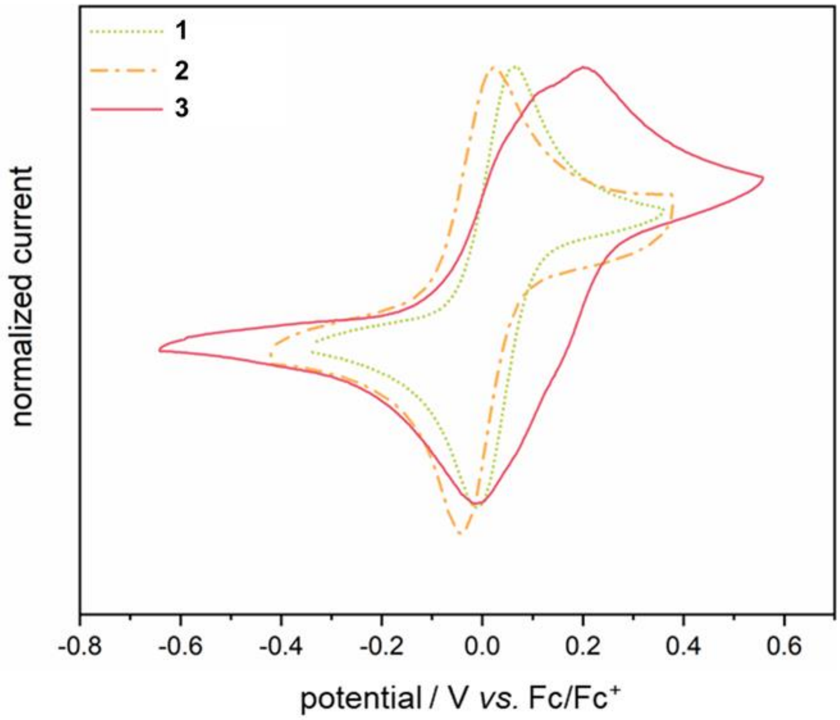

Fig. S22 Normalised cyclic voltammograms of **1** (green), **2** (orange) and **3** (red) recorded in 0.1 M [NBu$_4$][BArF$_{24}$]/CH_2Cl_2 for **3** and in 0.1 M [NBu$_4$][PF$_6$]/CH_2Cl_2 for **1** and **2** at a scan rate of 100 mV/s; values corrected for ohmic drop and reported *vs.* [Cp$_2$Fe]/[Cp$_2$Fe]$^+$.

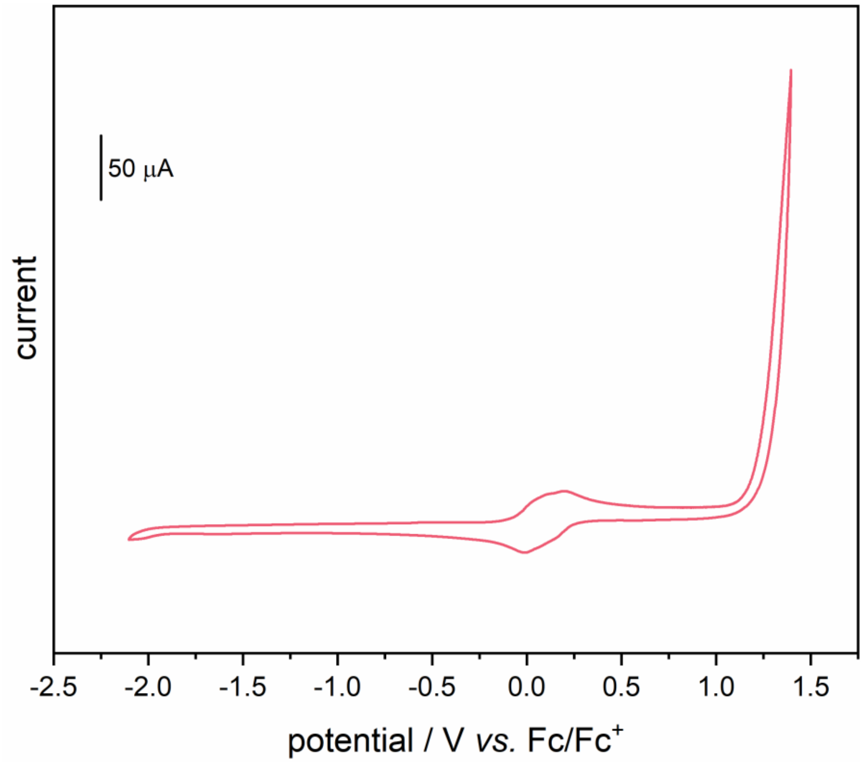

Fig. S23 Cyclic voltammogram of **3** with a large potential sweep in 0.1 M $[NBu_4][BArF_{24}]/CH_2Cl_2$ at 100 mV/s; values corrected for ohmic drop and reported *vs.* $[Cp_2Fe]/[Cp_2Fe]^+$.

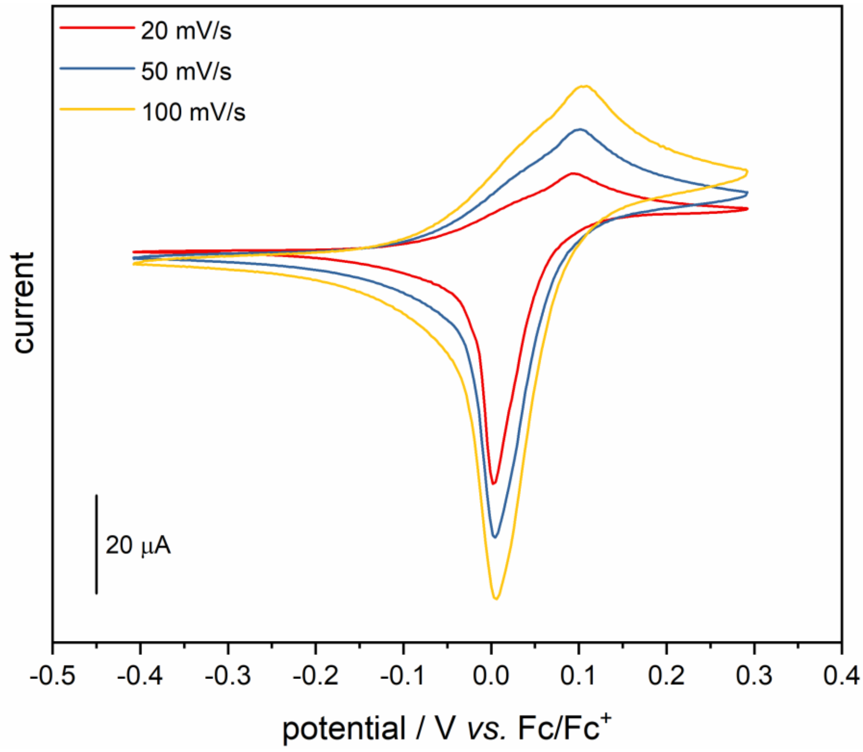

Fig. S24 Cyclic voltammograms of **3** in 0.1 M $[NBu_4][PF_6]/CH_2Cl_2$ at scan rates of 20, 50 and 100 mV/s; values corrected for ohmic drop and reported *vs.* $[Cp_2Fe]/[Cp_2Fe]^+$.

*Cyclic voltammograms of 2-pyrenylferrocene (**1**) at varied scan rates*

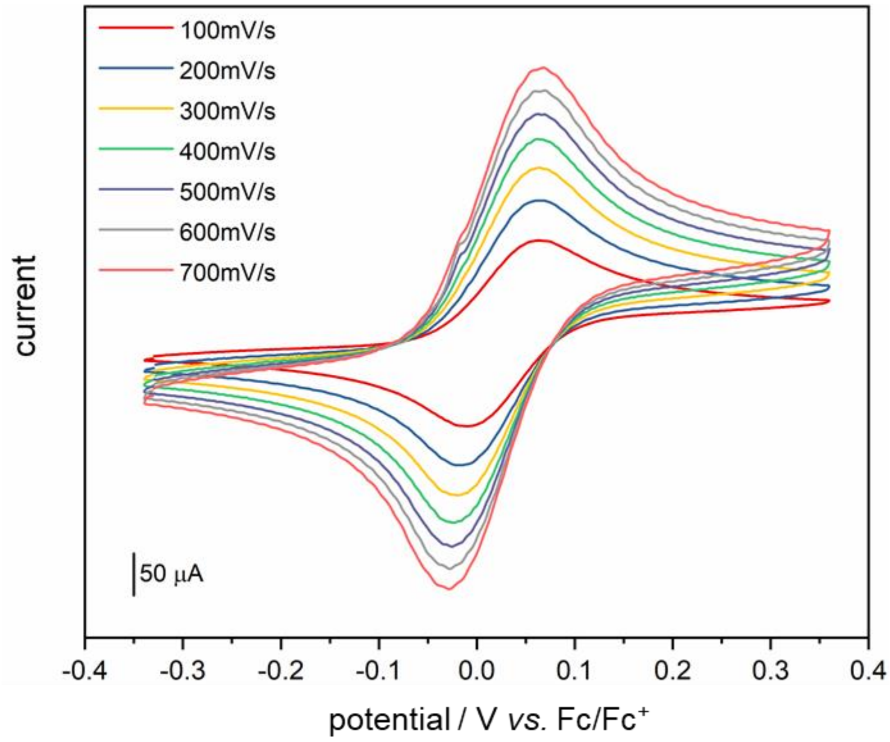

Fig. S25 Cyclic voltammograms with varying scan rates for **1** recorded in 0.1 M $[NBu_4][PF_6]/CH_2Cl_2$; values corrected for ohmic drop and reported *vs.* $[Cp_2Fe]/[Cp_2Fe]^+$.

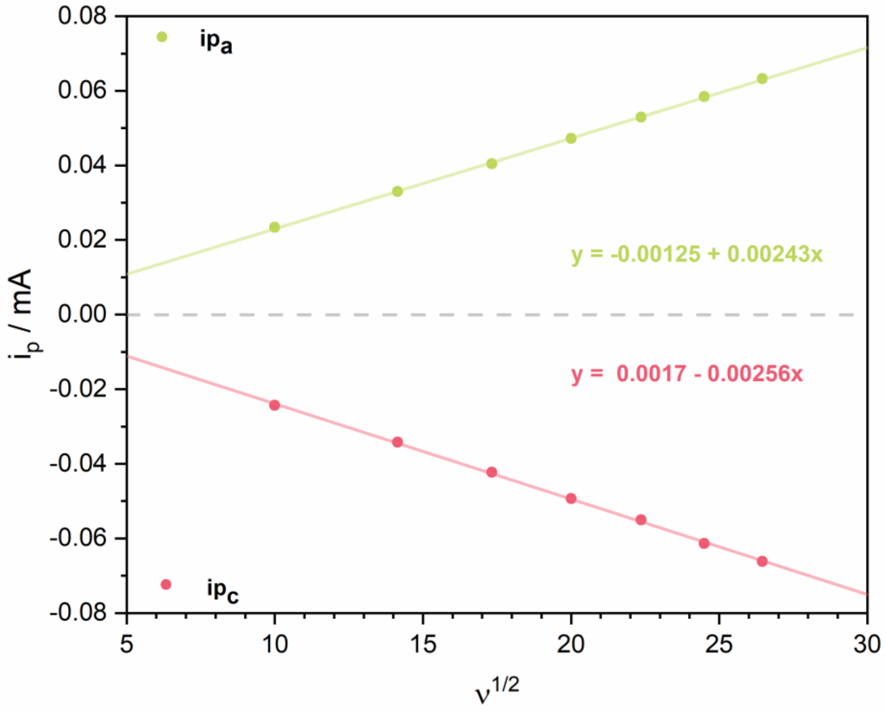

Fig. S26 Plot of peak currents i_{pa} (green) and i_{pc} (red) *vs.* $v^{1/2}$ for **1**. The data have been linearly fitted to demonstrate dependence according to Randles-Ševčík equation.

*Cyclic voltammograms of 1,1'-bis(2-pyrenyl)ferrocene (**2**) at varied scan rates*

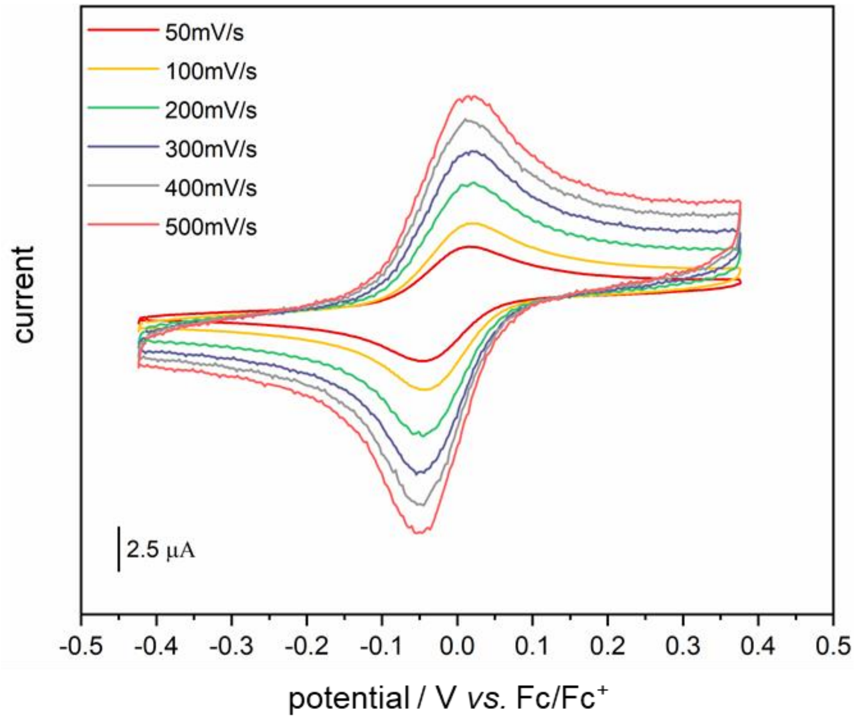

Fig. S27 Cyclic voltammograms with varying scan rates for **2** recorded in 0.1 M $[NBu_4][PF_6]/CH_2Cl_2$; values corrected for ohmic drop and reported *vs.* $[Cp_2Fe]/[Cp_2Fe]^+$.

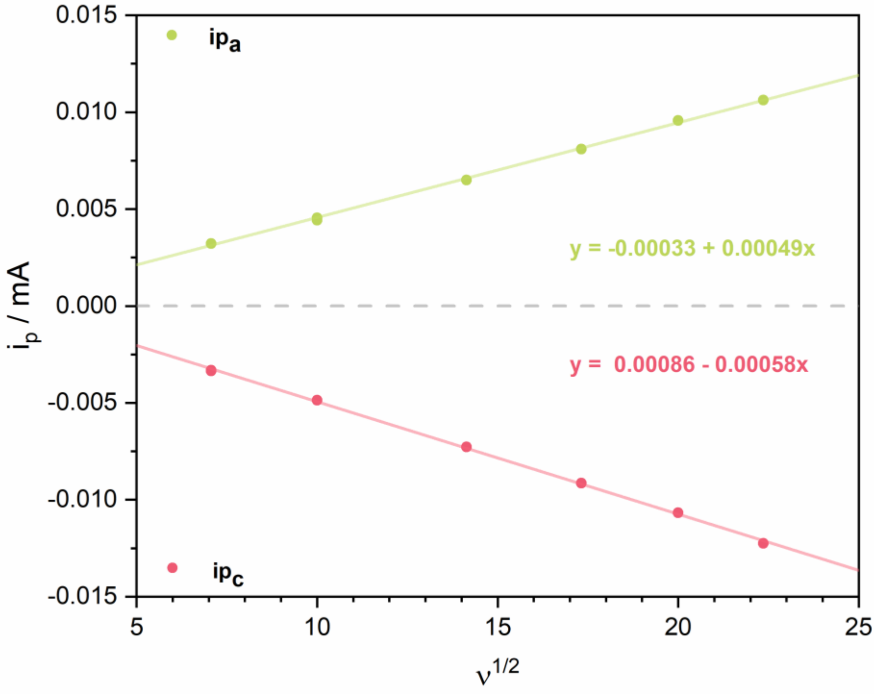

Fig. S28 Plot of peak currents i_{pa} (green) and i_{pc} (red) *vs.* $\nu^{1/2}$ for **2**. The data have been linearly fitted to demonstrate dependence according to Randles-Ševčík equation.

*Cyclic voltammograms of triangle **3** at varied scan rates*

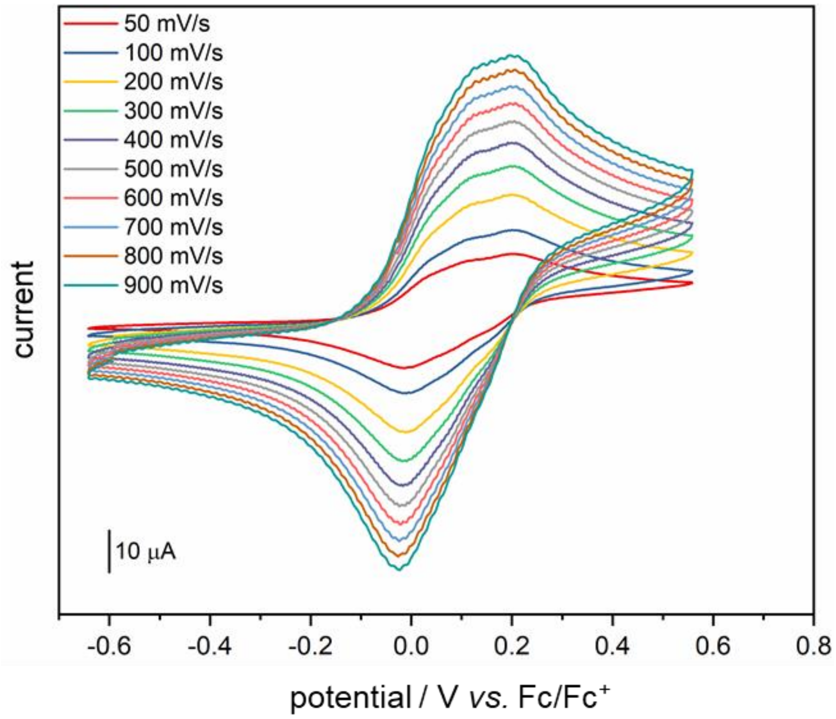

Fig. S29 Cyclic voltammograms with varying scan rates for **3** recorded in 0.1 M [NBu_4][$BArF_{24}$]/CH_2Cl_2; values corrected for ohmic drop and reported *vs.* [Cp_2Fe]/[Cp_2Fe]$^+$.

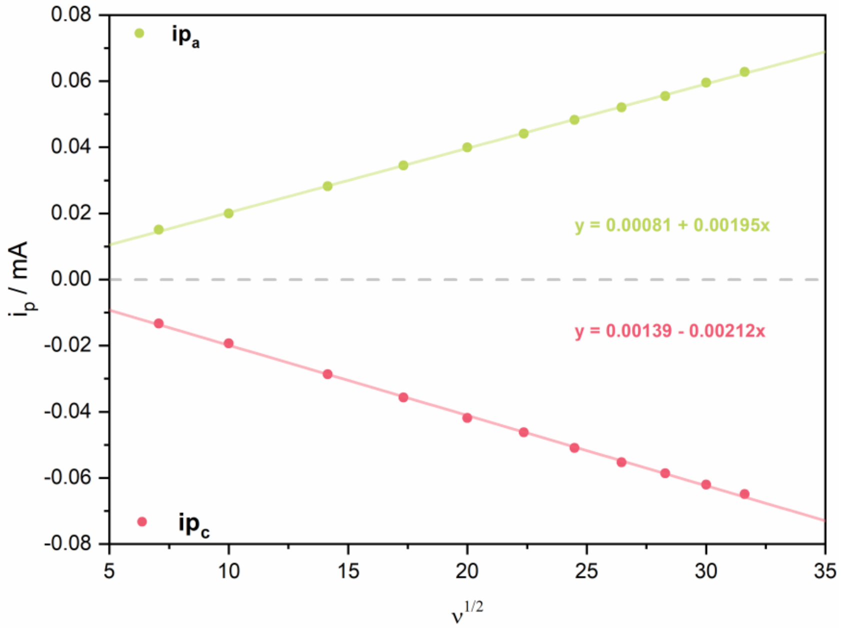

Fig. S30 Plot of peak currents i_{pa} (green) and i_{pc} (red) *vs.* $v^{1/2}$ for **3**. The data have been linearly fitted to demonstrate dependence according to Randles-Ševčík equation.

UV-Vis-NIR absorption spectra of 1 and 1^+

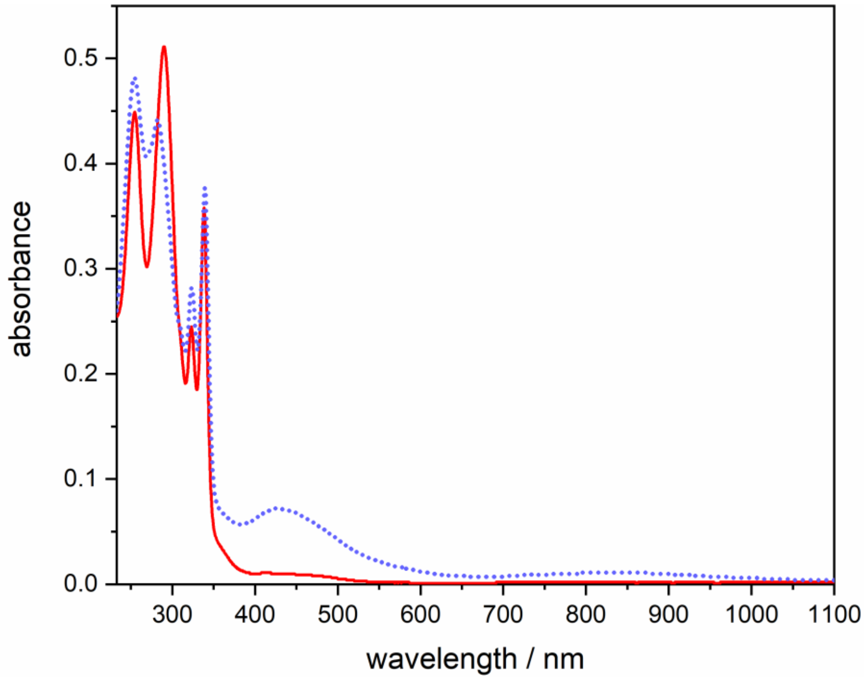

Fig. S31 UV-Vis-NIR absorption spectra of **1** (red) and $\mathbf{1}^+$ (dotted, blue) generated by addition of 1.0 equiv. $AgSbF_6$ in CH_2Cl_2. Note that no Na[$BArF_{24}$] electrolyte was used.

Circular dichroism (CD) absorption spectrum of 3

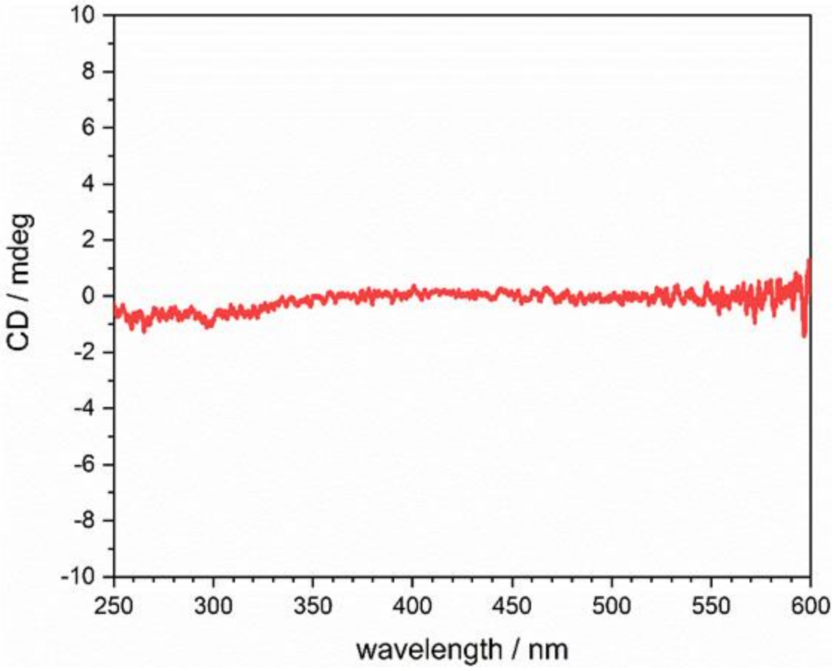

Fig. S32 CD absorption spectrum of **3** measured in CH_2Cl_2 at an absorbance of 0.93.

Single-crystal X-ray diffractometry

Orange crystals of **1** and **2** were grown by slow evaporation of $CHCl_3$ solutions. Orange crystals of **3** were grown by slow evaporation of toluene (**3·2Tol**), and by vapor diffusion method using THF as solvent and cyclohexane as antisolvent (**3·5THF**). Suitable single crystals were mounted on a Hampton Cryoloop using Paratone-N oil and diffraction data were collected on a SuperNova (Rigaku OD) diffractometer using Mo-Kα radiation (λ = 0.71073). Numerical absorption correction (Gaussian integration) was performed using CrysAlisPro (Rigaku OD).[9]

All structures were solved using SHELXT[10] (intrinsic phasing) and refined by full-matrix least-squares against $|F^2|$ using SHELXL[11] as implemented in Olex2.[12] Hydrogen atoms were added geometrically and refined using a riding model.

In compound **3·5THF**, the triangle **3** co-crystallises with five disordered THF molecules that were split and restrained to have the same internal distances within a standard uncertainty of 0.02 Å^2 for 1,2- and 0.04 Å for 1,3-distances (SADI). Atoms of disordered THF that are closer to one another than 1.7 Å were restrained to have the same components of anisotropic displacement parameters within a standard uncertainty of 0.01 Å^2 (SIMU). Rigid bond restraints with a standard uncertainty of 0.005 Å^2 were applied to one of the disordered THF molecules (DELU).[13]

Relevant crystallographic information for all compounds is summarised in Table S1 and supplementary crystallographic data are provided free of charge by the joint Cambridge Crystallographic Data Centre (CCDC) and Fachinformationszentrum (FIZ) Karlsruhe Access Structures service https://www.ccdc.cam.ac.uk/structures (CCDC deposition numbers 2076418 (**1**) and 2076419 (**2**), 2076420 (**3·5THF**), 2076421 (**3·2Tol**)). Crystal and molecular structures were visualised with CrystalMaker X[14] or VMD.[15]

Table S1. Crystallographic information for **1, 2**, **3·5THF** and **3·2Tol**.

	Compound **1**	Compound **2**	Compound **3·5THF**	Compound **3·2Tol**
empirical formula	$C_{26}H_{18}Fe$	$C_{42}H_{26}Fe$	$C_{98}H_{88}Fe_3O_5$	$C_{92}H_{64}Fe_3$
formula weight / g mol^{-1}	386.25	586.48	1513.23	1336.98
crystal size / mm^3	0.537 × 0.304 × 0.079	0.525 × 0.335 × 0.184	0.409 × 0.201 × 0.182	0.714 × 0.144 × 0.111
crystal system	orthorhombic	orthorhombic	triclinic	triclinic
space group	*Pbca*	*Pbca*	*P-1*	*P-1*
a / Å	15.6043(2)	20.87000(10)	11.4240(3)	11.6754(3)
b / Å	10.3677(2)	11.38260(10)	17.7656(4)	16.8491(3)
c / Å	21.3194(5)	22.14960(10)	18.4462(3)	16.8713(3)
α	90°	90°	78.866(2)°	84.071(2)°
β	90°	90°	79.702(2)°	71.467(2)°
γ	90°	90°	87.174(2)°	83.634(2)°
V / Å^3	3449.07(11)	5261.75(6)	3613.68(14)	3119.24(12)
Z	8	8	2	2
ρ_{calcd} / g cm^{-3}	1.488	1.481	1.391	1.423
μ / mm^{-1}	0.881	0.607	0.654	0.742
F(000)	1600.0	2432.0	1588.0	1388.0
T / K	100.05(10)	99.7(6)	100.3(3)	99.5(10)
radiation	Mo Kα (λ = 0.71073 Å)	Mo Kα (λ = 0.71073 Å)	Mo Kα (λ = 0.71073 Å)	Mo Kα (λ = 0.71073 Å)
2Θ range for data collection	6.536° to 58.356°	6.45° to 58.556°	6.816° to 59.522°	6.55° to 52.744°
index ranges	$-19 \le h \le 21$, $-13 \le k \le 13$, $-28 \le l \le 28$	$-28 \le h \le 28$, $-15 \le k \le 15$, $-28 \le l \le 30$	$-15 \le h \le 15$, $-24 \le k \le 24$, $-25 \le l \le 25$	$-13 \le h \le 14$, $-20 \le k \le 21$, $0 \le l \le 21$
reflections collected	20092	110031	80096	12730
independent reflections	4282 [R_{int} = 0.0545, R_{sigma} = 0.0545]	6970 [R_{int} = 0.0392, R_{sigma} = 0.0155]	18292 [R_{int} = 0.0619, R_{sigma} = 0.0669]	12730 [R_{int} = 0.0668, R_{sigma} = 0.0341]
data / restraints / parameters	4282 / 0 / 244	6970 / 0 / 388	18292 / 704 / 1149	12730 / 0 / 858
Goodness-of-fit on F^2	1.053	1.059	1.026	1.057
final R indexes [$I \ge 2\sigma(I)$]	R_1 = 0.0440, wR_2 = 0.821	R_1 = 0.0313, wR_2 = 0.0814	R_1 = 0.0551, wR_2 = 0.1143	R_1 = 0.0449, wR_2 = 0.1163
final R indexes [all data]	R_1 = 0.0776, wR_2 = 0.0967	R_1 = 0.0350, wR_2 = 0.0839	R_1 = 0.0929, wR_2 = 0.1349	R_1 = 0.0579, wR_2 = 0.1301
largest diff. peak/hole / e Å^{-3}	0.35 / –0.45	0.41 / –0.45	0.81 / –0.91	0.75 / –0.50

*Crystal structure of 1-pyrenylferrocene (**1**)*

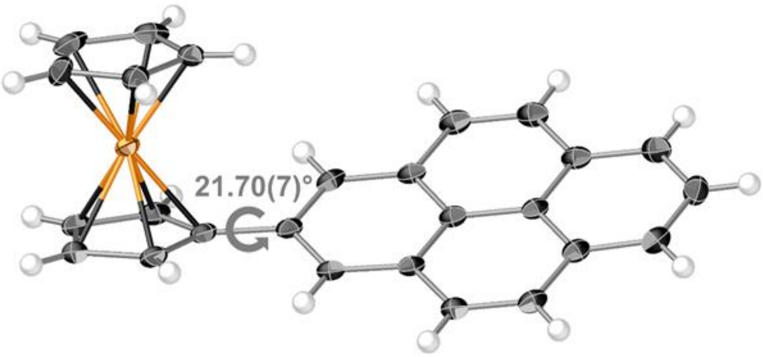

Fig. S33 Crystal structure of 2-pyrenylferrocene (**1**) represented with thermal ellipsoids (50% probability); the twisting angle between mean planes of Cp and pyrene is indicated in grey.

*Crystal structure of 1,1'-bis(2-pyrenyl)ferrocene (**2**)*

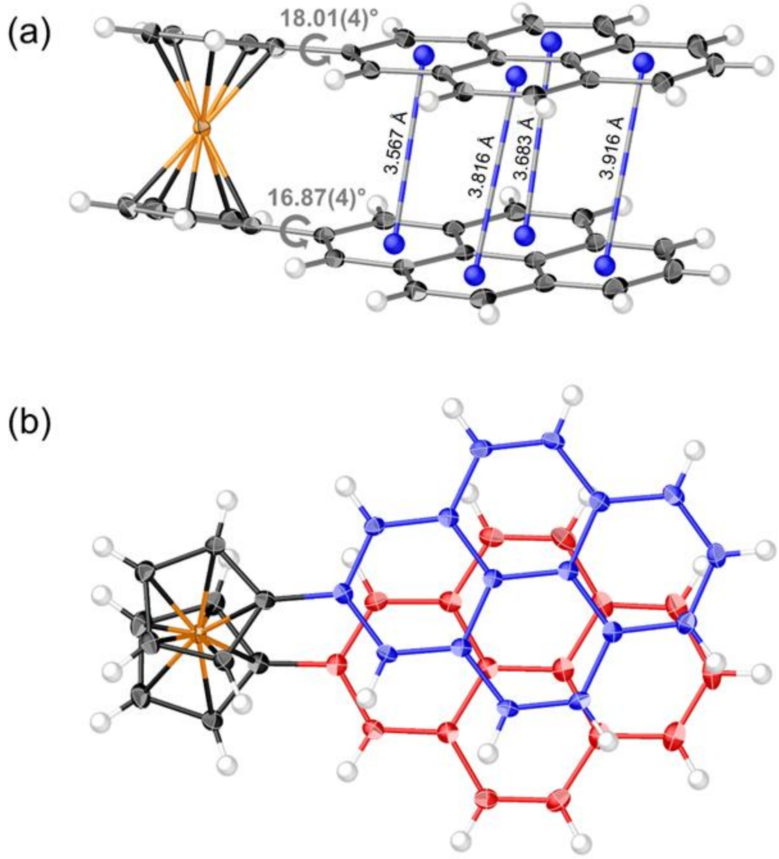

Fig. S34 Crystal structure of 1,1'-bis(2-pyrenyl)ferrocene (**2**) represented with thermal ellipsoids (50% probability) showing π-π interactions between the two pyrene groups; (a) edge-on, with distances between pyrene ring centroids (blue spheres) and twisting angles between mean planes of Cp and pyrene indicated in blue-grey and grey, respectively; (b) face-on, with the distal pyrene displayed in red and the proximal pyrene in blue.

*Crystal structure of triangle **3***

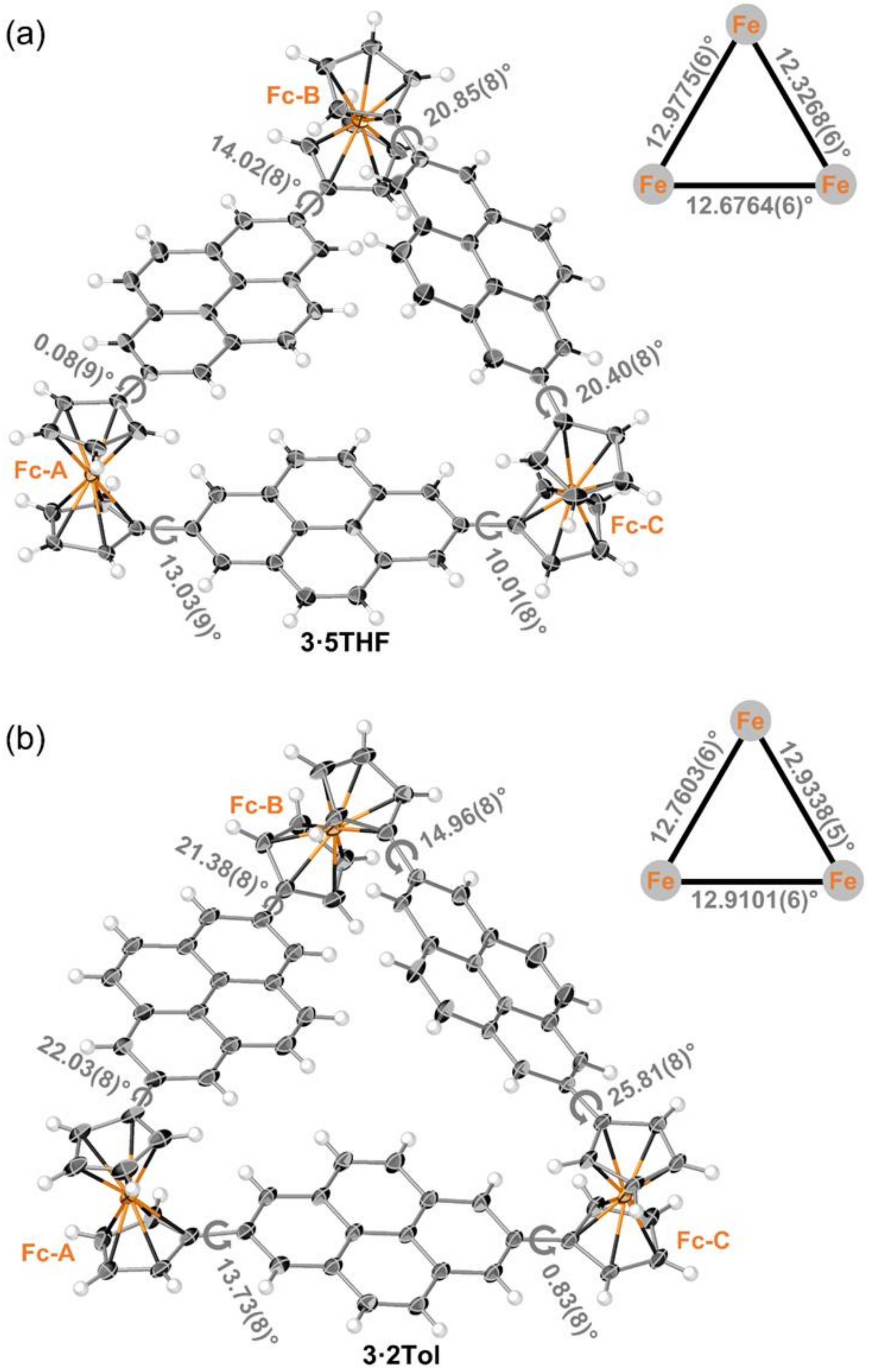

Fig. S35 Crystal structures of triangle **3** grown from (a) THF and (b) toluene, represented with thermal ellipsoids (50% probability); twisting angles between mean planes of Cp and pyrene are indicated in grey; insets: schematic representation of triangles **3·5THF** and **3·2Tol** with Fe···Fe distances shown in grey.

Main intermolecular interactions relevant in the crystal packing of ***3·5THF*** *and* ***3·2Tol***

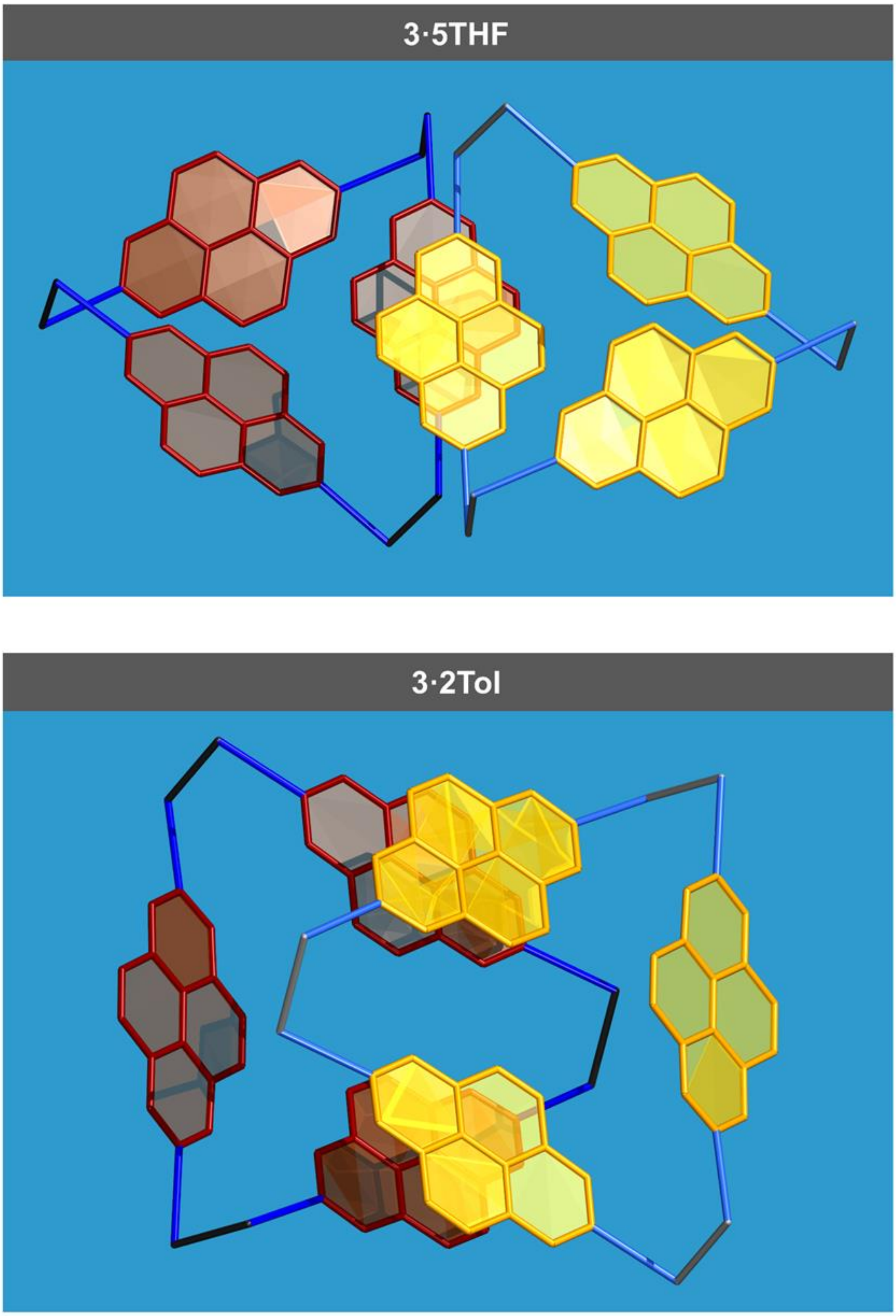

Fig. S36 Representation of the π-π contacts between molecules of **3·5THF** and **3·2Tol** taken from their crystal structures; ferrocene groups, hydrogen atoms, and crystallisation solvent have been omitted for clarity.

*Crystal packing motifs in **3·5THF***

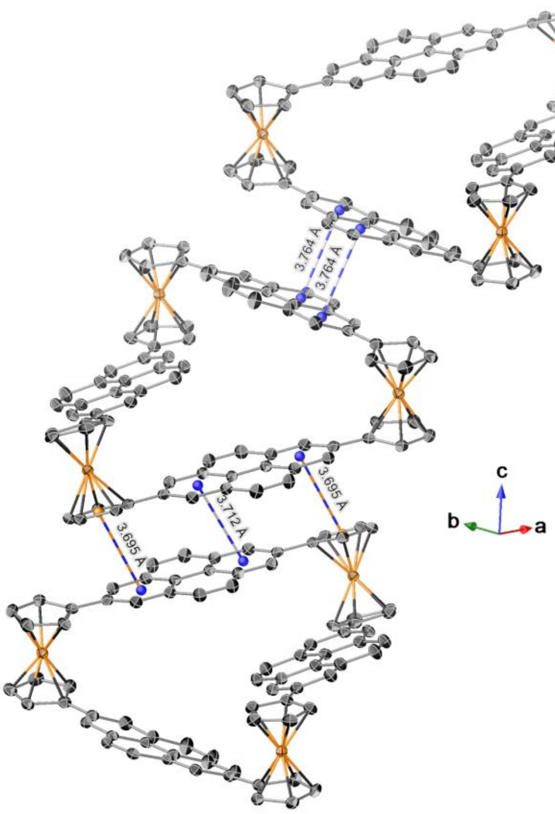

Fig. S37 Crystal packing of triangle **3·5THF** showing relevant intermolecular interactions between aromatic ring centroids (Py = blue, Cp = orange) as indicated by blue-grey/orange lines with corresponding distances. Molecules are displayed with thermal ellipsoids (50% probability). Solvent molecules, hydrogen atoms, and other surrounding molecules are omitted for clarity.

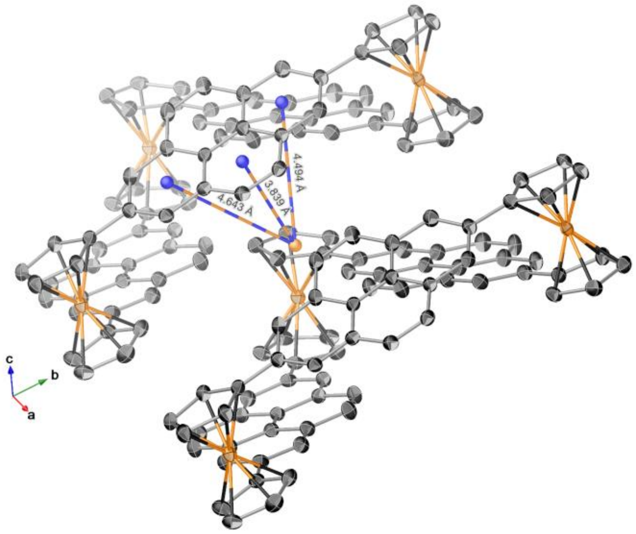

Fig. S38 Crystal packing of triangle **3·5THF** showing relevant intermolecular interactions between aromatic ring centroids (Py = blue, Cp = orange) as indicated by blue-orange lines with corresponding distances. Molecules are displayed with thermal ellipsoids (50% probability). Solvent molecules, hydrogen atoms, and other surrounding molecules are omitted for clarity.

*Crystal packing motifs in **3·2Tol***

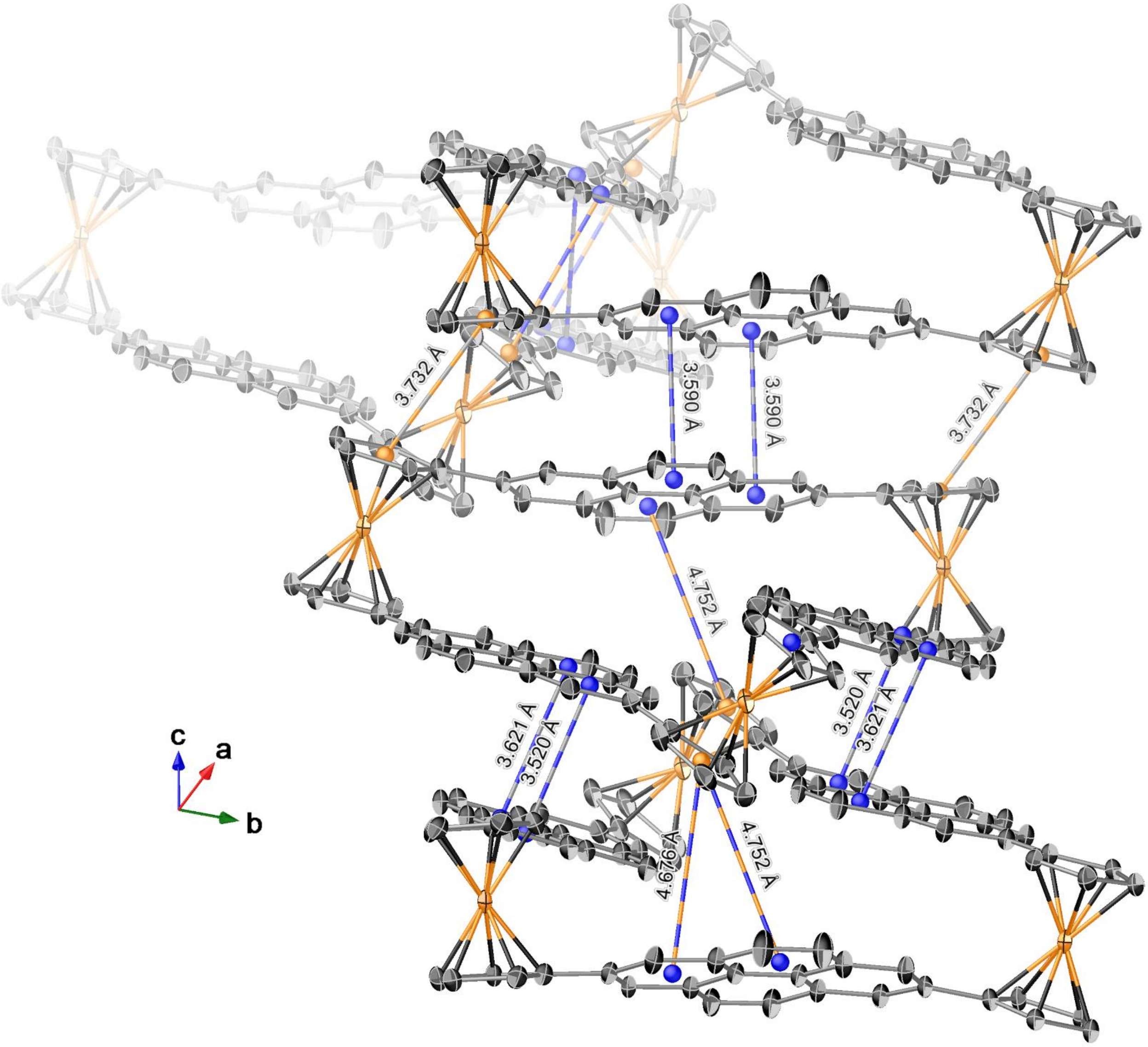

Fig. S39 Crystal packing of triangles in **3·2Tol** showing relevant intermolecular interactions between aromatic ring centroids (Py = blue, Cp = orange) as indicated by blue-grey/orange lines with corresponding distances. Molecules are displayed with thermal ellipsoids (50% probability). Solvent molecules, hydrogen atoms, and other surrounding molecules are omitted for clarity.

Conformer analysis for 3 *via* density functional theory (DFT)

We optimized the geometries of relevant conformers of **3** *via* density functional theory using the Gaussian 09 Rev. D.01[16] software package in tandem with GaussView 5.0.9. The Becke three-parameter hybrid exchange, and Lee-Yang-Parr correlation functionals (B3LYP)[17–21] were employed with a mixed basis set. For carbon and hydrogen, we used the Pople-style basis set 6-31G(d,p)[22–24], and for Fe atoms we used the Los Alamos National Lab 2 double-zeta (LANL2DZ)[25–27] effective core potential. Energy minima of all shown structures were verified by frequency calculations.

Relevant conformers of **3** are shown with their relative total energies in Fig. S40, and potential interconversion pathways are indicated by coloured arrows. The helical enantiomers with C_2 symmetry **3-A** (blue) and **3-A'** (green) that were observed in the crystal structure (see Fig. 1) are lowest in energy and can be interconverted by rotation of Fc-A (red) or Fc-B (blue arrow).

Geometry optimisations of homochiral, helical conformers of **3** revealed structures with C_3 (**3-C** and **3-C**') and D_3 symmetry (**3-D** and **3-D**') that exhibit higher relative energies of +30 and +41 kJ mol^{-1}, respectively, in comparison with **3-A/3-A'**. Partial rotation of the Fc-C and Py-B groups of **3-A/3-A'** (purple arrows in Fig. S40) results in an intermediate, C_2-symmetric conformer **3-B/3-B'** with a relative energy of +11 kJ mol^{-1}.

Fukino *et al.* reported a helical structure with D_3 symmetry for a similar ferrocene trimer based on NMR and CD experiments.[28] In the case of **3,** the lower Fe···Fe distances and close proximities of neighbouring pyrene groups favour conformers with C_2 symmetry in the gas and solid phase. We assume that the conformers **3-A/B** or **3-A'/B'** with C_2 symmetry predominate in solution because their energies are lower and because only one pathway leads to the formation of **3-B**/**C/D** or **3-B'/C'/D'** while three possible pathways are available for the back conversion to **3-A/3-A'** when considering rotation of only one Fc group. However, note that solvent effects and activation barriers for the interconversion of conformers Fig. S40 may play important and unknown roles to stabilize conformers in solution.

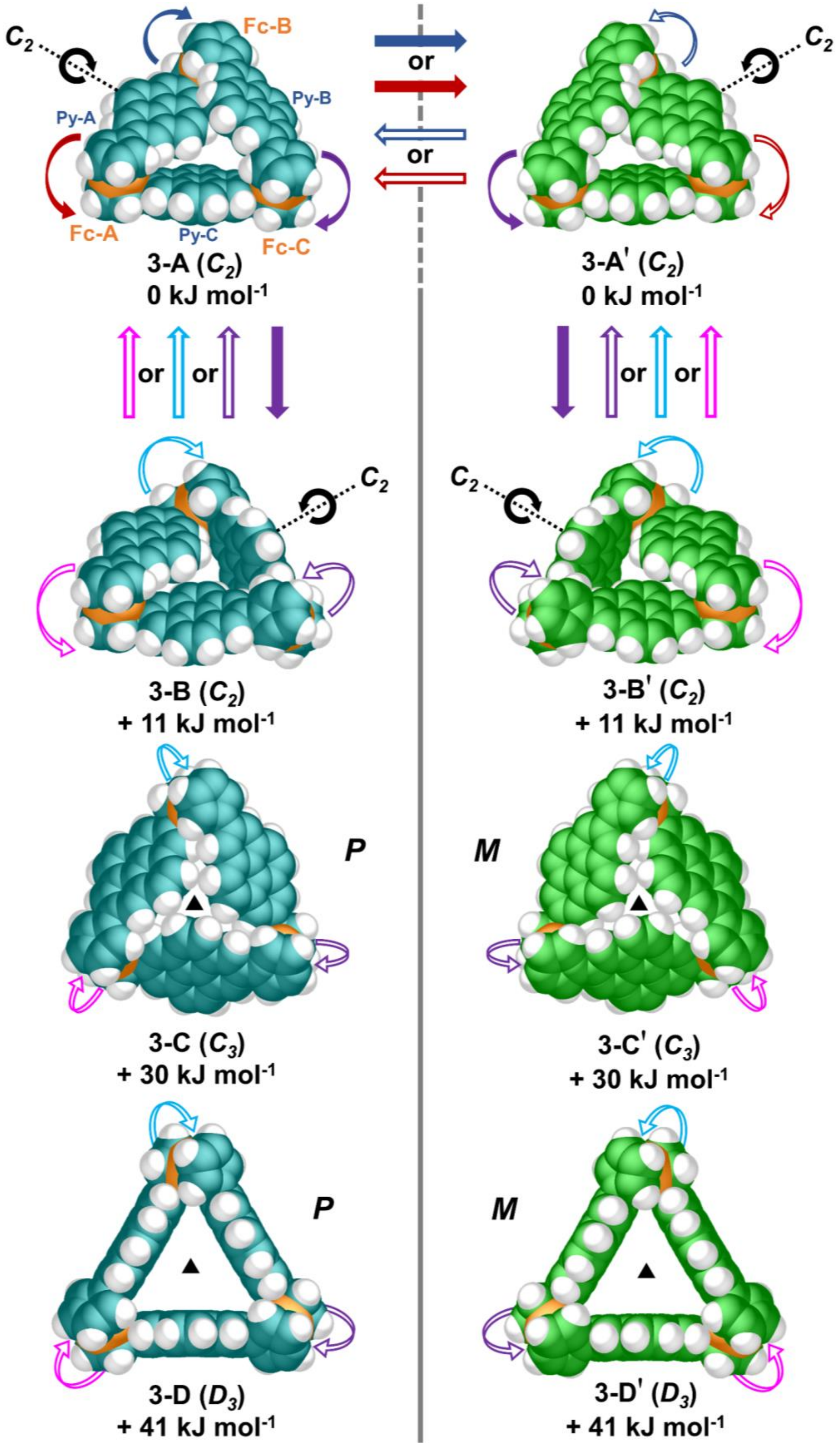

Fig. S40 Relevant conformers of triangle **3** optimized *via* DFT calculations using B3LYP functional with mixed basis set 6-31G(d,p)/LANL2DZ. Coloured arrows indicate interconversion pathways between conformers when assuming rotation of only one Fc group. Total energy values are reported relative to the energy of **3-A**/**3-A'**.

References

1 A. G. Crawford, Z. Liu, I. A. I. Mkhalid, M. H. Thibault, N. Schwarz, G. Alcaraz, A. Steffen, J. C. Collings, A. S. Batsanov, J. A. K. Howard and T. B. Marder, *Chem. Eur. J.*, 2012, **18**, 5022-5035.

2 M. Roemer and C. A. Nijhuis, *Dalton Trans.*, 2014, **43**, 11815-11818.

3 M. Metzelaars, S. Schleicher, T. Hattori, B. Bogdana, F. Matthes, S. Sanz, D. E. Bürgler, J. Rawson, C. M. Schneider and P. Kögerler, *Chem. Sci.*, 2021, *accepted*, DOI: 10.1039/D1SC01036K.

4 J. V. Olsen, B. Macek, O. Lange, A. Makarov, S. Horning and M. Mann, *Nat. Methods*, 2007, **4**, 709.

5 F. Barrière and W. E. Geiger, *J. Am. Chem. Soc.*, 2006, **128**, 3980-3989.

6 P. G. Gassman, J. R. Sowa, M. G. Hill and K. R. Mann, *Organometallics*, 1995, **14**, 4879-4885.

7 K. B. Vincent, J. B. G. Gluyas, Q. Zeng, D. S. Yufit, J. A. K. Howard, F. Hartl and P. J. Low, *Dalton Trans.*, 2017, **46**, 5522-5531.

8 J. B. G. Gluyas, A. J. Boden, S. G. Eaves, H. Yu and P. J. Low, *Dalton Trans.*, 2014, **43**, 6291-6294.

9 CrysAlisPro, Versions 1.171.38.46, 1.171.40.53, Rigaku Oxford Diffraction/Agilent Technologies UK Ltd, Yarnton (UK), 2015, 2019.

10 G. Sheldrick, *Acta Crystallogr. Sect. A: Found. Adv.*, 2015, **71**, 3-8.

11 G. Sheldrick, *Acta Crystallogr. Sect. C: Struct. Chem.*, 2015, **71**, 3-8.

12 O. V. Dolomanov, L. J. Bourhis, R. J. Gildea, J. A. K. Howard and H. Puschmann, *J. Appl. Crystallogr.*, 2009, **42**, 339-341.

13 P. Müller, R. Herbst-Irmer, A. L. Spek, T. R. Schneider and M. R. Sawaya, *Crystal Structure Refinement: A Crystallographer's Guide to SHELXL*, Oxford University Press, Oxford, 2006.

14 D. Palmer, A. Fernandez, M. Gao, CrystalMaker X Version 10.5.7, Program for Visualizing Crystal and Molecular Structures, CrystalMaker Software Ltd., Oxfordshire (UK), 2020.

15 W. Humphrey, A. Dalke and K. Schulten, *J. Mol. Graphics*, 1996, **14**, 33-38.

16 M. J. Frisch, G. W. Trucks, H. B. Schlegel, G. E. Scuseria, M. A. Robb, J. R. Cheeseman, G. Scalmani, V. Barone, B. Mennucci, G. A. Petersson, H. Nakatsuji, M. Caricato, X. Li, H. P. Hratchian, A. F. Izmaylov, J. Bloino, G. Zheng, J. L. Sonnenberg, M. Hada, M. Ehara, K. Toyota, R. Fukuda, J. Hasegawa, M. Ishida, T. Nakajima, Y. Honda, O. Kitao, H. Nakai, T. Vreven, J. A. Montgomery, Jr., J. E. Peralta, F. Ogliaro, M. Bearpark, J. J. Heyd, E. Brothers, K. N. Kudin, V. N. Staroverov, R. Kobayashi, J. Normand, K. Raghavachari, A. Rendell, J. C. Burant, S. S. Iyengar, J. Tomasi, M. Cossi, N. Rega, J. M. Millam, M. Klene, J. E. Knox, J. B. Cross, V. Bakken, C. Adamo, J. Jaramillo, R. Gomperts, R. E. Stratmann, O. Yazyev, A. J. Austin, R. Cammi, C. Pomelli, J. W. Ochterski, R. L. Martin, K. Morokuma, V. G. Zakrzewski, G. A. Voth, P. Salvador, J. J. Dannenberg, S. Dapprich, A. D. Daniels, Ö. Farkas, J. B. Foresman, J. V. Ortiz, J. Cioslowski, and D. J. Fox, *Gaussian 09 Rev. D.01*, Wallingford, CT, 2009.

17 C. Lee, W. Yang and R. G. Parr, *Phys. Rev. B*, 1988, **37**, 785-789.

18 B. Miehlich, A. Savin, H. Stoll and H. Preuss, *Chem. Phys. Lett.*, 1989, **157**, 200-206.

19 A. D. Becke, *J. Chem. Phys.*, 1993, **98**, 5648-5652.

20 P. J. Stephens, F. J. Devlin, C. F. Chabalowski and M. J. Frisch, *J. Phys. Chem.*, 1994, **98**, 11623-11627.

21 A. D. Becke, *Phys. Rev. A*, 1988, **38**, 3098-3100.

22 R. Ditchfield , W. J. Hehre and J. A. Pople, *J. Chem. Phys.*, 1971, **54**, 724-728.

23 W. J. Hehre, R. Ditchfield and J. A. Pople, *J. Chem. Phys.*, 1972, **56**, 2257-226.

24 P. C. Hariharan, J. A. Pople, *Theor. Chim. Acta*, 1973, **28**, 213-222.
25 P. J. Hay and W. R. Wadt, *J. Chem. Phys.*,1985, **82**, 270-83.
26 W. R. Wadt and P. J. Hay, *J. Chem. Phys.*, 1985, **82**, 284-98.
27 P. J. Hay and W. R. Wadt, *J. Chem. Phys.*, 1985, **82**, 299-310.
28 T. Fukino, N. Fujita and T. Aida, *Org. Lett.*, 2010, **12**, 3074-3077.